



**HAL**  
open science

## Seasonal radiative modeling of Titan's stratospheric temperatures at low latitudes

Bruno Bézard, Sandrine Vinatier, Richard K. Achterberg

► **To cite this version:**

Bruno Bézard, Sandrine Vinatier, Richard K. Achterberg. Seasonal radiative modeling of Titan's stratospheric temperatures at low latitudes. *Icarus*, 2018, 302, pp.437 - 450. 10.1016/j.icarus.2017.11.034 . hal-01671603

**HAL Id: hal-01671603**

<https://hal.sorbonne-universite.fr/hal-01671603v1>

Submitted on 22 Dec 2017

**HAL** is a multi-disciplinary open access archive for the deposit and dissemination of scientific research documents, whether they are published or not. The documents may come from teaching and research institutions in France or abroad, or from public or private research centers.

L'archive ouverte pluridisciplinaire **HAL**, est destinée au dépôt et à la diffusion de documents scientifiques de niveau recherche, publiés ou non, émanant des établissements d'enseignement et de recherche français ou étrangers, des laboratoires publics ou privés.

# Seasonal radiative modeling of Titan's stratospheric temperatures at low latitudes

Bruno Bézard<sup>a\*</sup>, Sandrine Vinatier<sup>a</sup>, Richard K. Achterberg<sup>b</sup>

<sup>a</sup>: LESIA, Observatoire de Paris, PSL Research University, CNRS, Sorbonne Universités, UPMC Univ. Paris 6, Université Paris-Diderot, Sorbonne Paris Cité, 5 place Jules Janssen, 92195 Meudon, France

<sup>b</sup>: University of Maryland, Department of Astronomy, College Park, MD 20742, United States

\* Corresponding author.

*E-mail address*: [bruno.bezard@obspm.fr](mailto:bruno.bezard@obspm.fr)

*Contact details*: Bruno Bézard  
LESIA, Bât. 18  
Observatoire de Paris, section de Meudon  
92195 Meudon cedex  
France

Phone: (33) 1 45 07 77 17

Fax: (33) 1 45 07 28 06

Published in *Icarus*, Volume 302, 1 March 2018, Pages 437–450  
<https://doi.org/10.1016/j.icarus.2017.11.034>

## ABSTRACT

1  
2  
3 We have developed a seasonal radiative-dynamical model of Titan's stratosphere to  
4 investigate the temporal variation of temperatures in the 0.2-4 mbar range observed by the  
5 Cassini/CIRS spectrometer. The model incorporates gas and aerosol vertical profiles derived  
6 from Cassini/CIRS and Huygens/DISR data to calculate the radiative heating and cooling rate  
7 profiles as a function of time and latitude. At 20°S in 2007, the heating rate is larger than the  
8 cooling rate at all altitudes, and more specifically by 20-35% in the 0.1-5 mbar range. A new  
9 calculation of the radiative relaxation time as a function of pressure level is presented, leading  
10 to time constants significantly lower than previous estimates. At 6°N around spring equinox,  
11 the radiative equilibrium profile is warmer than the observed one at all levels. Adding  
12 adiabatic cooling in the energy equation, with a vertical upward velocity profile  
13 approximately constant in pressure coordinates below the 0.02-mbar level (corresponding to  
14  $0.03\text{-}0.05\text{ cm s}^{-1}$  at 1 mbar), allows us to reproduce the observed profile quite well. The  
15 velocity profile above the  $\sim 0.5$ -mbar level is however affected by uncertainties in the haze  
16 density profile. The model shows that the change in insolation due to Saturn's orbital  
17 eccentricity is large enough to explain the observed 4-K decrease in equatorial temperatures  
18 around 1 mbar between 2009 and 2016. At 30°N and S, the radiative model predicts seasonal  
19 variations of temperature much larger than observed. A seasonal modulation of adiabatic  
20 cooling/heating is needed to reproduce the temperature variations observed from 2005 to 2016  
21 between 0.2 and 4 mbar. At 1 mbar, the derived vertical velocities vary in the range  $-0.05$   
22 (winter solstice) to  $0.16$  (summer solstice)  $\text{cm s}^{-1}$  at 30°S,  $-0.01$  (winter solstice) to  $0.14$   
23 (summer solstice)  $\text{cm s}^{-1}$  at 30°N, and  $0.03\text{-}0.07\text{ cm s}^{-1}$  at the equator.

24

25 Key words: Titan, atmosphere; Atmospheres, structure; Atmospheres, dynamics

26

27 **1. Introduction**

28 Due to Saturn's obliquity of  $26.7^\circ$ , Titan experiences large seasonal variations of insolation.

29 The 0.056 eccentricity of Saturn's orbit adds a significant modulation to this insolation.

30 Above the 10-mbar level, Titan's radiative time constant is less than a Titan year (29.5 Earth  
31 years) (Strobel et al. 2009, Flasar et al. 2014) so that significant seasonal variations of  
32 temperature are expected in the mid-stratosphere and mesosphere.

33

34 Infrared observations by the IRIS instrument aboard the Voyager 1 spacecraft in November  
35 1980 pointed out a north-to-south asymmetry of temperatures in the 0.4-1 mbar region, with  
36 temperatures at  $55^\circ\text{S}$  being higher than at  $55^\circ\text{N}$  by 4 and 8 K at 1 and 0.4 mbar respectively  
37 (Flasar et al. 1990). These observations occurred shortly after northern spring equinox, at a  
38 heliocentric longitude  $L_s \approx 9^\circ$ . Flasar and Conrath (1990) proposed that the asymmetry was  
39 due to a phase lag in the response of the atmosphere to the seasonally-varying insolation due  
40 to dynamical inertia. On the other hand, Bézard et al. (1995) suggested that the asymmetry  
41 results from the larger concentrations of infrared radiators (photochemical gases and aerosols)  
42 present at high northern latitudes.

43

44 The Cassini Composite Infrared Spectrometer (CIRS) aboard Cassini allowed us to monitor  
45 the thermal structure of Titan's stratosphere from July 2004 to September 2017, which  
46 corresponds to  $L_s \approx 293^\circ$ . Combining limb- and nadir-viewing observations between 2004 and  
47 2006, Achterberg et al. (2008a) retrieved the temperature field over the pressure range  $5 \times 10^{-3}$ -  
48 5 mbar from about  $75^\circ\text{S}$  to  $75^\circ\text{N}$ . The corresponding season was around northern mid-winter  
49 ( $L_s = 293$ - $323^\circ$ ). Compared with Voyager 1 observations, the north-to-south asymmetry was  
50 stronger and temperatures at  $55^\circ\text{S}$  were higher than at  $55^\circ\text{N}$  by about 18 and 11 K at 1 and 0.4  
51 mbar respectively. Compared to southern latitudes, high northern latitudes were then

52 experiencing reduced solar heating and enhanced abundances of photochemical gases and  
53 aerosols, both of which likely contribute to the lower temperatures. Besides this asymmetry,  
54 mid-stratosphere temperatures on Titan were reaching their maximum at latitudes 0-30°S. On  
55 the other hand, the stratopause was found higher and warmer beyond 50°N than anywhere  
56 else on the satellite, which very likely results from adiabatic heating from downwelling air at  
57 winter polar latitudes. Achterberg et al. (2011) extended the analysis of Achterberg et al.  
58 (2008a) using Cassini/CIRS data up to December 2009, i.e. shortly after northern spring  
59 equinox ( $L_s \approx 4^\circ$ ). Between 2004 and 2009, a large decrease of temperatures in the stratopause  
60 region (above the 0.1-mbar level) was found beyond 30°N. Elsewhere in the stratosphere and  
61 lower mesosphere, the temperature variations did not exceed 5 K.

62

63 The temporal and latitudinal variations of temperature observed in the stratosphere and lower  
64 mesosphere result from combined variations of the insolation, modulating the solar heating  
65 rate, of the atmospheric composition, which governs the radiative cooling and solar heating  
66 rates, and of dynamical motions, which provide adiabatic heating and cooling. To try to assess  
67 the relative importance of these actors, it is first necessary to constrain as precisely as possible  
68 the radiative forcing terms, which requires a good knowledge of the distribution of the  
69 radiatively-active gases and aerosols. Such information is available from Cassini/CIRS, which  
70 measures in nadir- and limb-viewing geometry the thermal emission spectrum of Titan from  
71 10 to  $1495 \text{ cm}^{-1}$ . This allows the retrieval of the gas concentration and aerosol extinction  
72 profiles that contribute to the radiative cooling between approximately 130 and 450 km (5-  
73 0.005 mbar) (e.g. Vinatier et al. 2010a, 2010b, 2015). The Descent Imager/Spectral  
74 Radiometer (DISR) aboard the Huygens probe measured the optical properties and vertical  
75 distribution of haze particles between 0 and  $\approx 150$  km (Tomasko et al. 2008c, Doose et al.  
76 2016) on 14 January 2005 near 10°S. Used with a correct representation of the methane

77 opacity, these results allow us to compute the solar heating rate profile as a function of zenith  
78 angle. Combining Huygens/DISR and Cassini/CIRS data, Tomasko et al. (2008b) were able  
79 to investigate the heat balance at the location and time of the Huygens descent. They inferred  
80 that the day-averaged solar heating rate profile exceeded the cooling rate profile by a  
81 maximum of 0.5 K/Titan day (0.03 K/Earth day) near 120 km altitude (5.5 mbar) and  
82 concluded that the general circulation must redistribute this heat to higher latitudes.  
83  
84 In Titan's stratosphere, a meridional circulation, similar to Hadley cells on Earth, is driven by  
85 the latitude-dependent solar heating (see a review of Titan's general circulation in Lebonnois  
86 et al. 2014). General Circulation Models (GCMs) have been developed to investigate Titan's  
87 dynamics, in particular the superrotation characterized by prograde zonal winds up to  $\sim 200$  m  
88  $s^{-1}$  in the winter stratosphere (see Newman et al. 2011, Lebonnois et al. 2012 and Lora et al.  
89 2015 for recent three-dimensional GCMs). These models show a pole-to-pole circulation,  
90 particularly in the stratosphere, with rising motion in the summer hemisphere and subsidence  
91 in the winter hemisphere except around equinox, when a more symmetric equator-to-pole  
92 circulation takes place throughout the atmosphere. They generally succeed in reproducing at  
93 least qualitatively the dominant features of Titan's atmospheric structure, such as the zonal  
94 wind pattern and temperature field, but suffer from approximations in the treatment of the  
95 radiative transfer and/or various other simplifications. The strong subsidence at high winter  
96 latitudes predicted by the GCMs is confirmed by the high temperatures and the large  
97 enrichment in minor photochemical species observed in the upper stratosphere and  
98 mesosphere (Achterberg et al. 2011; Teanby et al. 2007, 2009; Vinatier et al. 2007, 2010a).  
99 The temperature anomalies observed in winter around the north pole have been used to  
100 estimate downward vertical velocities of  $\sim 10$  cm  $s^{-1}$  around 0.01 mbar in 2005-2007  
101 (Achterberg et al. 2011). Changes in the vertical abundance profiles of minor species

102 observed near the south pole in autumn were also used to derive the following vertical  
103 velocities: from 0.1 to 0.4 cm s<sup>-1</sup> near 0.003 mbar in 2010-2011 and 2011-2012 (Teanby et al.  
104 2012, Vinatier et al. 2015), 0.25 cm s<sup>-1</sup> near 0.01 mbar in 2011-2012, and 0.4 cm s<sup>-1</sup> near 0.02  
105 mbar in 2015 (Vinatier et al. 2017a).

106

107 The goal of this paper is to investigate the heat balance of Titan's stratosphere using a  
108 seasonal radiative model based on measurements by Cassini/CIRS of the distributions of the  
109 radiative agents and state-of-the-art representation of gas and aerosol spectral properties. We  
110 also take into account constraints from Huygens/DISR measurements. We then calculate the  
111 season-dependent radiative solution for the temperature profile and compare it with the  
112 observed variations of temperature at different levels and latitudes to derive constraints on the  
113 dynamical heating/cooling. Here, we restrain our analysis to mid-latitudes (30°S-30°N) where  
114 gas and aerosol do not exhibit large seasonal variations. Section 2 describes the temperature  
115 data, retrieved from Cassini/CIRS measurements, with which we are comparing our model.  
116 Section 3 presents our seasonal radiative model and the gas and aerosol distributions used in  
117 the radiative transfer code to calculate heating and cooling rates. Radiative model results are  
118 presented in Section 4 and compared with observations to constrain the missing adiabatic  
119 heating and cooling terms. Also shown is a calculation of the radiative time constant as a  
120 function of pressure level. We discuss these results in Section 5 and present our conclusions  
121 in Section 6.

122

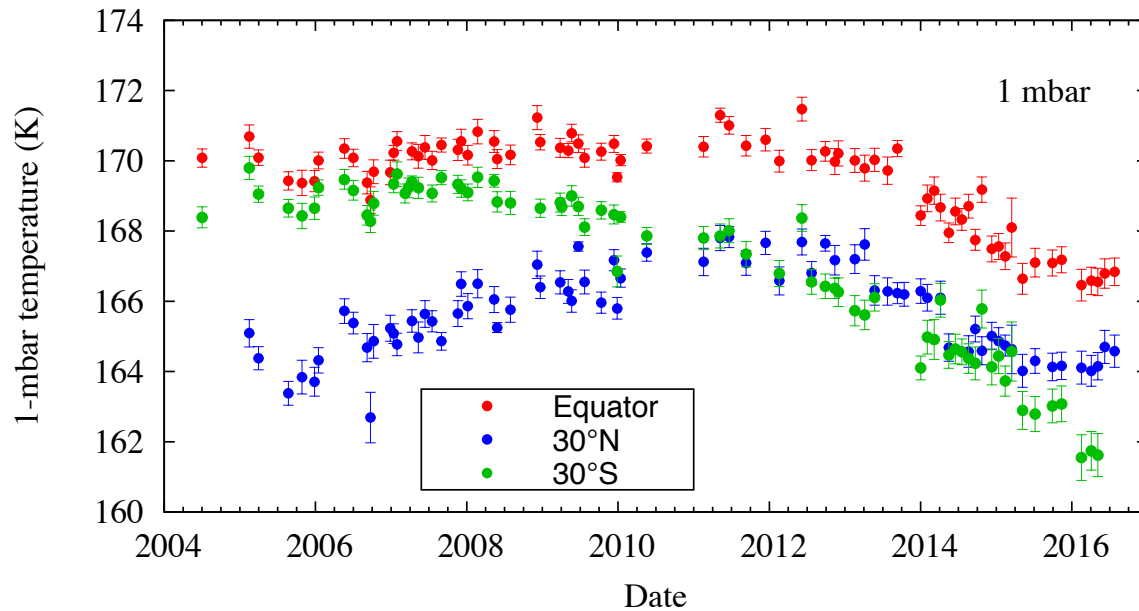
## 123 **2. Observations**

124 Retrievals of Titan's temperature field are routinely achieved using nadir and limb  
125 observations of the  $\nu_4$  band of methane through Focal Plane FP4 of Cassini/CIRS. This focal  
126 plane covers the interval 1050-1495 cm<sup>-1</sup> at a spectral resolution adjustable from 15.5 to 0.5

127  $\text{cm}^{-1}$  (apodized). It consists of a 10-pixel linear array, with a 0.27-mrad field of view (FOV)  
128 per pixel (Flasar et al. 2004). Temperature maps were retrieved by Achterberg et al. (2008a)  
129 for mid-winter conditions (2004-2006) combining nadir-viewing ( $2.8\text{-cm}^{-1}$  resolution) and  
130 limb-viewing ( $15.5\text{-cm}^{-1}$  resolution) sequences. The nadir data cover latitudes from  $90^{\circ}\text{S}$  to  
131  $60^{\circ}\text{N}$  and yield information in a pressure range of about 5-0.2 mbar while the limb data cover  
132 latitudes from  $75^{\circ}\text{S}$  to  $85^{\circ}\text{N}$  and yield information in a pressure range  $\approx 1\text{-}0.005$  mbar.  
133 Achterberg et al. (2011) extended the analysis to cover 5.5 years of Cassini/CIRS  
134 observations from July 2004 to December 2009, just after northern spring equinox. Here we  
135 use a further extended data set encompassing observations up to June 2016, i.e. Titan flybys  
136 T0 to T118 (Achterberg et al. in preparation). For each flyby, zonal-mean temperatures were  
137 obtained by zonally averaging temperatures retrieved from individual nadir-viewing spectra  
138 ( $2.8\text{-cm}^{-1}$  resolution) using  $5^{\circ}$  latitude bins with  $2.5^{\circ}$  spacing and interpolating the retrieved  
139 temperatures onto a uniform latitude grid for each flyby. Averaging was done in a reference  
140 frame that removes the  $4^{\circ}$  offset of the stratospheric symmetry axis from the surface pole  
141 (Achterberg et al. 2008b). In our analysis, we used temperatures retrieved at 0.2, 0.5, 1, 2 and  
142 4 mbar, which cover the range of maximum temperature information. Note that these  
143 temperatures actually represent a vertical average over 1 to 1.5 scale heights due to the width  
144 of the contribution functions in the methane band and the filtering applied in the retrieval  
145 process. We restrained our analysis to equatorial and mid-latitudes and selected data at  $\theta = 0^{\circ}$ ,  
146  $30^{\circ}\text{N}$  and  $30^{\circ}\text{S}$ . For a given latitude  $\theta$  and a given flyby, we averaged the three temperatures  
147 retrieved by Achterberg et al. (in preparation) at latitudes  $\theta-2.5^{\circ}$ ,  $\theta$  and  $\theta+2.5^{\circ}$ . Figure 1  
148 shows the retrieved 1-mbar temperatures as a function of time for these three latitudes. The  
149 error bars correspond to the standard deviation (SD) of temperatures in each  $5^{\circ}$  bin divided by  
150 square of root of the number of data points. Seasonal variations are clearly visible in this data  
151 set. At the equator, the 1-mbar ( $\sim 185$  km) temperature increases slightly from 2005 to 2011-



152 2012 (by less than 1 K), and decreases more noticeably after 2012 (by  $\sim 4$  K between 2012  
 153 and 2016). At  $30^\circ\text{N}$ , the temperature increases by  $\sim 4$  K from 2005 to 2012 and decreases by  
 154 about the same amount from 2012 to 2016, while at  $30^\circ\text{S}$  the temperature regularly decreases  
 155 by  $\sim 8$  K from 2005 to 2016.



156

**Figure 1:** Time variation of 1-mbar temperatures retrieved from Cassini/CIRS measurements at three latitudes,  $0^\circ$ ,  $30^\circ\text{N}$  and  $30^\circ\text{S}$ .

157

158 Vinatier et al. (2015) produced maps of temperature and composition from selected sequences  
 159 of CIRS limb spectra recorded between October 2006 and May 2013 at a resolution of either  
 160  $0.5$  or  $15.5 \text{ cm}^{-1}$ . Reliable information extends from 5 to 0.001 mbar, a region below which  
 161 the temperature profile smoothly joins the Huygens/HASI profile measured *in situ* at  $10^\circ\text{S}$  in  
 162 January 2005 (Fulchignoni et al. 2005). We used Vinatier et al.'s results around  $6^\circ\text{N}$ , a  
 163 latitude least sensitive to seasonal effects, as a reference profile to test our model and  
 164 investigate the heat balance at this latitude. To smooth out small local temperature variations,  
 165 we averaged four temperature profiles recorded at  $4\text{--}5^\circ\text{N}$ , on January 2007 ( $L_s = 327^\circ$ ),  
 166 December 2009 ( $L_s = 4^\circ$ ), June 2010 ( $L_s = 11^\circ$ ) and May 2011 ( $L_s = 21^\circ$ ), thus corresponding  
 167 to northern mid-winter to mid-spring conditions. This profile is shown in Fig. 7. The 1-SD

168 formal error bar due to noise propagation is about  $\pm 0.2$  K in the range 0.1-1 mbar increasing  
 169 to  $\pm 0.3$  K at 0.01 mbar and  $\pm 0.4$  K at 5 mbar. The standard deviation of our set of four  
 170 temperature profiles is larger, 0.5 to 1.5 K from 0.2 to 2 mbar, 2 K at 0.1 and 5 mbar and 5 K  
 171 at 0.01 mbar.

172

### 173 **3. Seasonal radiative model**

174 We developed a one-dimensional seasonal radiative-dynamical model to investigate the  
 175 observed temperature variations in Titan's stratosphere. We solve for the energy equation:

$$176 \quad \frac{\partial T(z)}{\partial t} = h(z) - c(z) - w(z) \left( \frac{g(z)}{c_p} + \frac{\partial T(z)}{\partial z} \right). \quad (1)$$

177  $h(z)$  is the solar heating rate equal to  $-\frac{g}{c_p} \frac{dF_*(p)}{dp}$ , where  $F_*$  is the downward solar flux,  $c(z)$  is

178 the radiative cooling rate equal to  $-\frac{g}{c_p} \frac{dF_{IR}(p)}{dp}$  with  $F_{IR}$  being the upward thermal emission

179 flux,  $w$  the upward vertical velocity,  $C_p$  the specific heat, and  $g$  the acceleration of gravity.

180 The term  $w(z) \frac{g(z)}{c_p}$  represents the adiabatic cooling rate and  $w(z) \frac{\partial T(z)}{\partial z}$  the cooling rate due to

181 vertical advection. The solar flux is calculated for diurnally averaged (i.e. zonally-averaged)

182 insolation. We neglect the meridional advection of heat. As discussed by Achterberg et al.

183 (2011) and Teanby et al. (2017), this term is expected to be  $\leq 0.2$  time the vertical advection

184 term, based on the mass continuity equation and the observed horizontal temperature

185 gradients, all the more at low latitudes where these temperature gradients are very small.

186

#### 187 *3.1 Solar flux*

188 Our atmospheric grid consists of 41 pressure levels uniformly distributed in log-scale from

189 1.466 bar (surface pressure) to 0.133  $\mu$ bar (around 650 km). The solar flux is calculated as a

190 function of zenith angle  $\theta$ , and altitude from 2610 to 40000  $\text{cm}^{-1}$  (3.8-0.25  $\mu\text{m}$ ) using a plane

191 parallel radiative transfer code that incorporates the DISORT algorithm (Stamnes et al. 1988)

192 with 8 streams to solve for scattering. The solar irradiance spectrum at 1 AU is the 2000  
 193 ASTM Standard Extraterrestrial Spectrum Reference E-490-00 (available at  
 194 <http://rredc.nrel.gov/solar/spectra/am0/>). We consider opacity from methane and aerosols.  
 195 Methane absorption is modeled from  $2610 \text{ cm}^{-1}$  ( $3.8 \text{ }\mu\text{m}$ ) to  $25000 \text{ cm}^{-1}$  ( $0.400 \text{ }\mu\text{m}$ ) using the  
 196 correlated- $k$  distribution method. From  $2690$  to  $11850 \text{ cm}^{-1}$ , absorption coefficients are  
 197 calculated with a line-by-line radiative transfer model and molecular line parameters  
 198 (positions, intensities, energy levels) from the TheoReTS database, which includes new  
 199 accurate theoretical linelists of  $^{12}\text{CH}_4$ ,  $^{13}\text{CH}_4$  and  $^{12}\text{CH}_3\text{D}$  (Rey et al. 2017). The assumed  $\text{N}_2$ -  
 200 broadened halfwidths and far wing lineshape are described in Rey et al. The  $\text{CH}_3\text{D}/\text{CH}_4$  ratio  
 201 corresponds to  $\text{D}/\text{H} = 1.32 \times 10^{-4}$  (Bézard et al. 2007). For each  $40\text{-cm}^{-1}$  interval, a set of 16  $k$ -  
 202 coefficients, 8 for the interval  $[0:0.95]$  of the normalized frequency  $g$  and 8 for the interval  
 203  $[0.95:1.00]$ , is calculated on a set of pressures and temperatures. Beyond  $11850 \text{ cm}^{-1}$ , we used  
 204 the coefficients of the Voigt-Goody band model calculated by Karkoschka and Tomasko  
 205 (2010, Table 4) based on methane transmission measurements from laboratory, Huygens and  
 206 HST data. We then essentially proceeded as in Irwin et al. (1996) and generated, for each  
 207 pressure and temperature of our set, 24 transmission ( $T_r$ ) spectra with column densities ( $a$ )  
 208 equally spaced in log space between a minimum value such as  $T_r \approx 0.997$  and a maximum  
 209 value such as  $T_r \leq 0.01$ . This function  $T_r(a)$  was then fitted with an exponential sum  
 210 characterized by 10-point Gaussian Legendre quadrature abscissae and weights, using a  
 211 Levenberg-Marquardt non-linear least squares algorithm (Press et al. 1997). The first guess of  
 212 the 10  $k_i$  absorption coefficients was derived from the  $k$  distribution of a Malkmus-Lorentz  
 213 band model (Eq. 12 of Irwin et al. 1996) having the  $S$  and  $B$  parameters given in Table 4 of  
 214 Karkoschka and Tomasko (2010). The function  $T_r(a)$  was actually fitted with the 10  
 215 parameters  $k_i$  and  $(k_i - k_{i-1})$ , for  $i = 2, 10$ , discarding the iterations leading to negative values of  
 216 any of them, to ensure that they increase monotonically. We kept the original sampling of

217 Karkoschka and Tomasko (2010):  $5 \text{ cm}^{-1}$  in the interval  $11850\text{-}19300 \text{ cm}^{-1}$  and  $25 \text{ cm}^{-1}$  in the  
 218 interval  $19300\text{-}25000 \text{ cm}^{-1}$ .

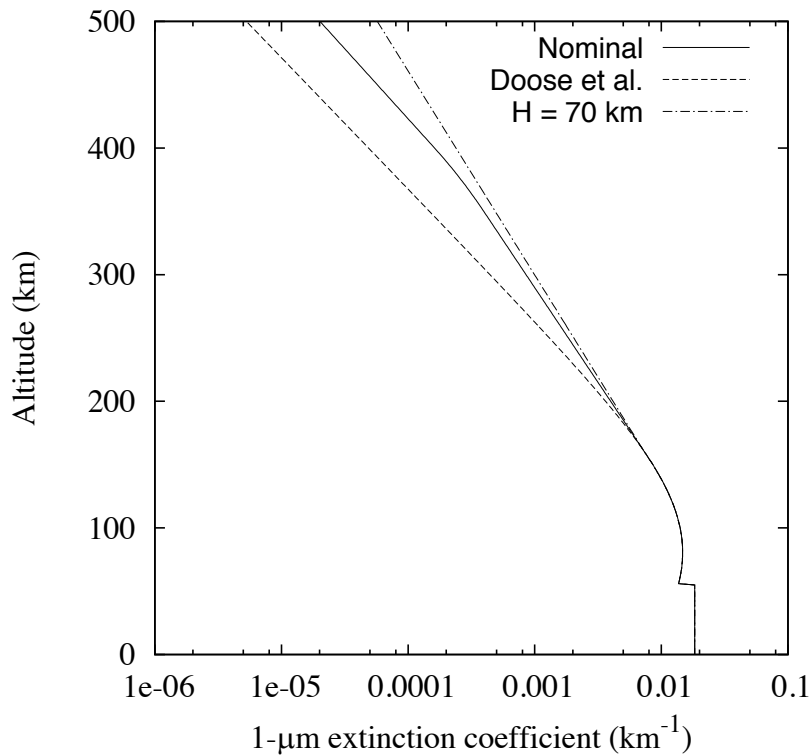


**Figure 2:** Haze extinction coefficient at  $1 \mu\text{m}$  for our nominal model (solid line), Doose et al.'s (2016) model (dashed line) and one with a constant scale height of 70 km above 160 km (dash-dot line). In the thermal infrared range, at  $1090 \text{ cm}^{-1}$ , these extinction profiles are scaled by factors of 0.0103, 0.0113 and 0.0099 respectively.

219

220 The methane mole fraction profile used in the radiative transfer is that derived by Niemann et  
 221 al. (2010) from the analysis of Huygens/GCMS in situ measurements, with a uniform mole  
 222 fraction of  $1.48 \times 10^{-2}$  above 45 km. The temperature profile  $T_0(p)$  is that retrieved by Vinatier  
 223 et al. (2010a) from Cassini/CIRS limb and nadir spectra recorded near  $20^\circ\text{S}$  in March 2007,  
 224 not far from the Huygens descent latitude.

225

226 The properties of the aerosol particles (single scattering albedo, phase function) were taken  
 227 from the recent reanalysis of Huygens/DISR observations by Doose et al. (2016, Table 2)

228 with information on the phase function from Tomasko et al. (2008c). Longward of 950 nm,  
229 we used the single scattering albedo derived by Hirtzig et al. (2013) from modeling of  
230 Cassini/VIMS data. We used the wavelength dependence of the extinction given in Table 2 of  
231 Doose et al. (2016). The vertical variation of the extinction at the Huygens site is constrained  
232 in detail between 0 and 144 km from the DISR measurements but only in average above this  
233 altitude. Doose et al. then added the additional constraint of the optical limb altitude as  
234 observed by Karkoschka and Lorenz (1997) to produce an analytical vertical profile of  
235 extinction characterized, in the stratosphere, by an optical depth scale height decreasing from  
236 large values below 80 km to a value of 65 km at 120 km and an asymptotic value of 45 km at  
237 very high altitudes (Fig. 2). Here we considered additional constraints from Cassini/CIRS  
238 measurements of the aerosol continuum emission in limb-viewing and nadir geometry  
239 between 600 and 1500  $\text{cm}^{-1}$ . These measurements provide a vertical profile of the extinction  
240 at thermal wavelengths with a good precision between approximately 140 and 400 km (3-0.01  
241 mbar) (Vinatier et al. 2010b, 2015). We used here the vertical dependence of the extinction  
242 determined from limb observations in January 2007 around 5°N (Vinatier et al. 2010a, b) and  
243 adapted by Vinatier et al. (2015) (dashed line in their Fig. 15). Their extinction profile has a  
244 scale height ( $H$ ) of about  $\sim 65$  km up to 350 km decreasing to  $\sim 48$  km above 400 km. Our  
245 nominal profile for the haze extinction is then the Doose et al. profile up to 160 km, that we  
246 extend above with  $H = 65$  km from 160 to 350 km, linearly decreasing to 48 km at 400 km  
247 (Fig. 2). The extinction profiles derived from CIRS measurements at equatorial and mid-  
248 latitudes show however a significant variability with latitude and year above 250 km (Vinatier  
249 et al. 2015, 2016). Although part of it may be an artifact due to uncertainties in the continuum  
250 calibration, especially at high altitudes ( $\geq 400$  km), most of it is probably real, including the  
251 presence of the variable detached haze layer, as discussed in Vinatier et al. (2015). An  
252 average of the profiles observed in 2010-2012 between 20°N and 30°S (Fig. 15 of Vinatier et

253 al. 2015) shows a vertical variation close to the Doose et al. profile up to 300 km and  
 254 intermediate between our nominal profile and Doose et al. up to 400 km. On the other hand,  
 255 observations at 26°S in January 2016 exhibit an approximately constant scale height  $H$  as  
 256 large as 70 km between 200 and 500 km (Vinatier et al. 2016). We consider that the full  
 257 Doose et al. profile and one having  $H = 70$  km above 160 km represent a reasonable envelope  
 258 of the actual extinction profiles at low latitudes (Fig. 2).

259

260 We assumed a Lambertian surface with the reflectivity inferred by Jacquemart et al. (2008)  
 261 between 900 and 1600 nm from DISR/DLIS spectra taken at an altitude of 25 m and after  
 262 landing of the Huygens probe. The surface reflectivity down to 400 nm was obtained from  
 263 Eq. 5 of Karkoschka et al. (2012), giving the relative spectral variation of I/F derived from  
 264 DISR/DLVS data after landing, and scaled with the Jacquemart et al. value at 900 nm.  
 265 Between 250 and 400 nm, we assumed a linear variation of  $4 \times 10^{-4} \text{ nm}^{-1}$  and, beyond 1600  
 266 nm, we used the Hirtzig et al. (2013) albedos derived from the methane windows in  
 267 Cassini/VIMS spectra near the Huygens landing site. We account neither for the strong  
 268 opposition effect seen in the phase function of Titan's surface (Karkoschka et al. 2012) nor  
 269 for the fact that the surface at Huygens' landing site is darker than average at low latitudes.  
 270 However, the influence of the surface reflectivity on the heating rate at stratospheric levels  
 271 should be relatively low.

272

### 273 *3.2 Thermal emission*

274 Without scattering, the thermal flux at pressure level  $p$  is equal to:

$$275 F_{IR}(p) = 2\pi \int_0^\infty d\sigma \left[ \int_{\tau_\sigma}^\infty B_\sigma(T(\tau'_\sigma)) E_2(\tau'_\sigma - \tau_\sigma) d\tau'_\sigma - \int_0^{\tau_\sigma} B_\sigma(T(\tau'_\sigma)) E_2(\tau_\sigma - \tau'_\sigma) d\tau'_\sigma \right], \quad (2)$$

276 where  $\tau_\sigma$  is the optical depth at wavenumber  $\sigma$  and pressure level  $p$ ,  $B_\sigma(\tau'_\sigma)$  is the Planck  
 277 function at the temperature  $T$  of the level of optical depth  $\tau'_\sigma$  and wavenumber  $\sigma$ , and  $E_2$  is

278 the second-order exponential integral ( $E_2(x) = \int_1^\infty \frac{e^{-xt}}{t^2} dt$ ). The two terms in Eq. 2 represent  
 279 the fluxes from respectively the upwelling and downwelling radiation at pressure level  $p$ . We  
 280 calculate this integral from 20 to 1560  $\text{cm}^{-1}$ , and divide it into  $n_k = 74$  intervals of width  $\delta\sigma =$   
 281 20  $\text{cm}^{-1}$ . Thermal emission from outside this spectral interval can be neglected in the energy  
 282 budget. Our grid has  $n_p = 51$  pressure levels uniformly distributed in log-scale from  $p_1$   
 283 = 1.466 bar (surface pressure) to  $p_{n_p} = 0.1466 \mu\text{bar}$  (around 650 km). By linearizing the  
 284 Planck function as a function of optical depth within each atmospheric layer of our grid [ $j,$   
 285  $j+1$ ], and assuming that the Planck function is constant over each spectral interval  $k$  of width  
 286  $\delta\sigma$ , i.e.:

$$287 \quad B_{\sigma_k}(T(\tau'_\sigma)) = B_{\sigma_k}(T(p_j)) \frac{\tau_\sigma(p_{j+1}) - \tau'_\sigma}{\tau_\sigma(p_{j+1}) - \tau_\sigma(p_j)} + B_{\sigma_k}(T(p_{j+1})) \frac{\tau'_\sigma - \tau_\sigma(p_j)}{\tau_\sigma(p_{j+1}) - \tau_\sigma(p_j)}, \quad (3)$$

288 Eq. 2 at a given pressure level  $p_i$  can be written out as summations over indices  $k$  and  $j$  as:

$$289 \quad F_{IR}(p_i) = \pi \delta\sigma \sum_{k=1}^{n_k} \left[ \frac{B_{\sigma_k}(T(p_1))}{\delta\sigma} \int_{\sigma_k - \delta\sigma/2}^{\sigma_k + \delta\sigma/2} 2E_2(\tau_\sigma(p_1) - \tau_\sigma(p_i)) d\sigma + \right. \\
 290 \quad \left. \sum_{j=1}^{i-1} \frac{1}{\delta\sigma} \int_{\sigma_k - \delta\sigma/2}^{\sigma_k + \delta\sigma/2} d\sigma \int_{\tau_\sigma(p_{j+1})}^{\tau_\sigma(p_j)} B_{\sigma_k}(T(\tau'_\sigma)) 2E_2(\tau'_\sigma - \tau_\sigma(p_i)) d\tau'_\sigma - \right. \\
 291 \quad \left. \sum_{j=i}^{n_p-1} \frac{1}{\delta\sigma} \int_{\sigma_k - \delta\sigma/2}^{\sigma_k + \delta\sigma/2} d\sigma \int_{\tau_\sigma(p_{j+1})}^{\tau_\sigma(p_j)} B_{\sigma_k}(T(\tau'_\sigma)) 2E_2(\tau_\sigma(p_i) - \tau'_\sigma) d\tau'_\sigma \right], \quad (4)$$

292 where the first term in the summation over  $k$  is the contribution from the surface, the second  
 293 one that from atmospheric layers below level  $i$  and the third one that from atmospheric layers  
 294 above level  $i$ . Combining Eqs. 3 and 4 allows us to express the flux at pressure level  $p_i$  as a  
 295 linear combination of the Planck functions at the  $n_p$  pressure levels ( $p_j$ ) and  $n_k$  wavenumbers  
 296 ( $\sigma_k$ ):

$$297 \quad F_{IR}(p_i) = \pi \delta\sigma \sum_{k=1}^{n_k} \sum_{j=1}^{n_p} B_{\sigma_k}(T(p_j)) A_{i,j,k}, \quad (5)$$

298 where  $A_{i,j,k}$  is a dimensionless coupling factor between levels  $p_i$  and  $p_j$  for the  $k^{\text{th}}$  frequency  
 299 interval. We calculated this exchange matrix  $A$  for the reference temperature profile  $T_0(p)$  (see

300 above) and neglect its dependence on temperature in our seasonal model, given that it is  
301 generally much weaker than that of the Planck function.

302

303 The exchange matrix  $A$  was calculated through a line-by-line radiative transfer program that  
304 incorporates opacity from the collision-induced absorption (CIA) of N<sub>2</sub>-H<sub>2</sub>-CH<sub>4</sub> pairs, lines  
305 from CH<sub>4</sub>, CH<sub>3</sub>D, C<sub>2</sub>H<sub>6</sub>, C<sub>2</sub>H<sub>2</sub>, C<sub>2</sub>H<sub>4</sub>, CH<sub>3</sub>C<sub>2</sub>H, C<sub>4</sub>H<sub>2</sub>, C<sub>3</sub>H<sub>8</sub>, CO, CO<sub>2</sub> and HCN, and aerosols.  
306 Spectroscopic line parameters are described in Vinatier et al. (2010a) with, in addition, C<sub>2</sub>H<sub>6</sub>  
307 lines in the 7- $\mu$ m region from HITRAN2012 (Rothman et al. 2013), the CH<sub>3</sub>C<sub>2</sub>H bands  
308 around 15.5 and 30  $\mu$ m from Geisa2011 (Jacquinet-Husson et al. 2011), and rotational lines  
309 from CH<sub>4</sub>, CO and HCN as described in Lellouch et al. (2014). Line parameters of C<sub>4</sub>H<sub>2</sub>  
310 bands were updated following Geisa2011. References for the CIA coefficients are given in  
311 Vinatier et al. (2007), with the N<sub>2</sub>-CH<sub>4</sub> coefficients multiplied by a factor of 1.5, following  
312 Tomasko et al. (2008b). For the main haze opacity, we utilized the spectral dependence of the  
313 extinction cross section derived from Cassini/CIRS measurements by Vinatier et al. (2012)  
314 from 600 to 1500 cm<sup>-1</sup> and by Anderson and Samuelson (2011) at shorter wavenumbers.

315

316 We used the vertical profiles of C<sub>2</sub>H<sub>6</sub>, C<sub>2</sub>H<sub>2</sub>, C<sub>2</sub>H<sub>4</sub>, CH<sub>3</sub>C<sub>2</sub>H, C<sub>4</sub>H<sub>2</sub>, C<sub>3</sub>H<sub>8</sub>, and HCN derived  
317 by Vinatier et al. (2010a) from limb measurements near 20°S in March 2007<sup>1</sup>. As for the  
318 calculation of the solar flux, the CH<sub>4</sub> profile is that of Niemann et al. (2010) and the CH<sub>3</sub>D  
319 profile derives from D/H = 1.32  $\times$  10<sup>-4</sup> (Bézard et al. 2007). The CO<sub>2</sub> and CO mole fractions  
320 were held constant at 1.6  $\times$  10<sup>-8</sup> and 4.7  $\times$  10<sup>-5</sup> respectively (de Kok et al. 2007).

321

322 We assumed a uniform composition from 30°S to 30°N and constant throughout the mission.

323 This is consistent with monitoring studies based on Cassini/CIRS nadir observations by

---

<sup>1</sup> Temperature and abundance profiles available from the Virtual European Solar and Planetary Access (VESPA) <http://vespa.obspm.fr/planetary/data/epn/query/all/>



324 Teanby et al. (2008) and Coustenis et al. (2013), which all show limited variations of  
 325 composition at latitudes less than  $30^\circ$  in the  $\sim 2$ -10 mbar region. As shown later,  $C_2H_2$ ,  $C_2H_6$   
 326 and  $CH_4$  are the main gaseous cooling agents. Compiling the  $C_2H_2$  and  $C_2H_6$  profiles retrieved  
 327 from CIRS limb and nadir observations from 2007 to 2016 by Vinatier et al. (2010a, 2015,  
 328 2017b), we have calculated the standard deviation (SD) of the mole fractions in these sets at  
 329 levels between 0.5 and 2 mbar. We found a SD of about 10% of the mean value for  $C_2H_6$ ,  
 330 which is about the 1-SD uncertainty of the retrievals, and 15-20% of the mean value for  $C_2H_2$ ,  
 331 which is only marginally larger than the retrieval uncertainty.

332

333 The vertical profile of haze extinction is the one described above to model the solar flux  
 334 deposition, scaled to a value of  $4.1 \times 10^{-10} \text{ cm}^{-1}$  at 200 km and  $1090 \text{ cm}^{-1}$  as derived by  
 335 Vinatier et al. (2015) in the  $30^\circ\text{S}$ - $20^\circ\text{N}$  region in 2010-2012. We added the opacity of the  
 336 nitrile haze characterized by Anderson and Samuelson (2011). The spectral dependence of  
 337 this opacity at  $15^\circ\text{S}$  is given in Fig. 15 of that paper; it peaks at  $160 \text{ cm}^{-1}$  and is significant in  
 338 the range  $90$ - $290 \text{ cm}^{-1}$ . We used a normal optical depth of  $0.0054$  at  $160 \text{ cm}^{-1}$ , as derived by  
 339 Anderson and Samuelson (2011) at  $15^\circ\text{S}$ , and the associated vertical profile of extinction,  
 340 having a mass extinction coefficient peaking at 87.5 km with a full width at half maximum  
 341 (FWHM) of 18.8 km.

342

### 343 *3.3 Numerical aspects*

344 Starting from the initial temperature profile  $T_0(p)$ , Eq. 1 is integrated through a time-marching  
 345 scheme, with a constant step  $\Delta\xi$  (typically  $10^{-3}$ ),  $\xi$  being related to the time  $t$ , Sun distance  $d$   
 346 and heliocentric longitude  $\phi$  through the relations (Landau and Lifchitz 1969, Eqs. (15,10)  
 347 and (15,11)):

$$348 \quad t = \frac{T_{orb}}{2\pi} (\xi - e \sin \xi), \quad 6(a)$$

349  $d = a(1 - e \cos \xi),$  6(b)

350  $\cos \phi = \frac{\cos \xi - e}{1 - e \cos \xi},$  6(c)

351 where  $T_{orb}$  is Saturn's orbital period,  $e$  its orbit eccentricity,  $a$  its semi-major axis, with the  
 352 origin of time and longitude taken at perihelion ( $\xi = 0, t = 0, \phi = 0$ ). Note that the heliocentric  
 353 longitude with an origin at northern spring equinox  $L_s$  is then equal to  $\phi + L_s^0$ ,  $L_s^0$  being the  
 354 value of  $L_s$  at perihelion. The solar declination  $\delta_s$  is given by:

355  $\sin \delta_s = \sin \delta \sin L_s,$  6(d)

356 where  $\delta$  is Saturn's obliquity.

357

358 The time-marching integration is run for long enough so that the influence of the initial  
 359 profile  $T_0(p)$  has vanished at the end. At each time step, the diurnally averaged solar flux is  
 360 derived for the corresponding solar declination and Sun-Saturn distance by integrating over  
 361 daytime and interpolating as a function of  $\cos(\theta_s)$  from the solar fluxes pre-calculated for  
 362 zenith angles  $\theta_s = 0, 30, 50, 60, 70, 80$  and  $85^\circ$  (Section 3.1). The thermal flux is calculated  
 363 from Eq. 5, assuming as a boundary condition a constant surface temperature of 93.5 K and  
 364 emissivity of 1.0. Radiative cooling and heating rates are then calculated on the atmospheric  
 365 pressure grid by differentiation of the solar and thermal fluxes. After adding the adiabatic and  
 366 advective cooling/heating terms in Eq. 1 to the radiative terms, the variation of temperature  
 367  $\Delta T$  at each level is calculated from Eq. 1 as  $\Delta t$  times the sum of these three energy terms, and  
 368 the process is iterated till the desired date.

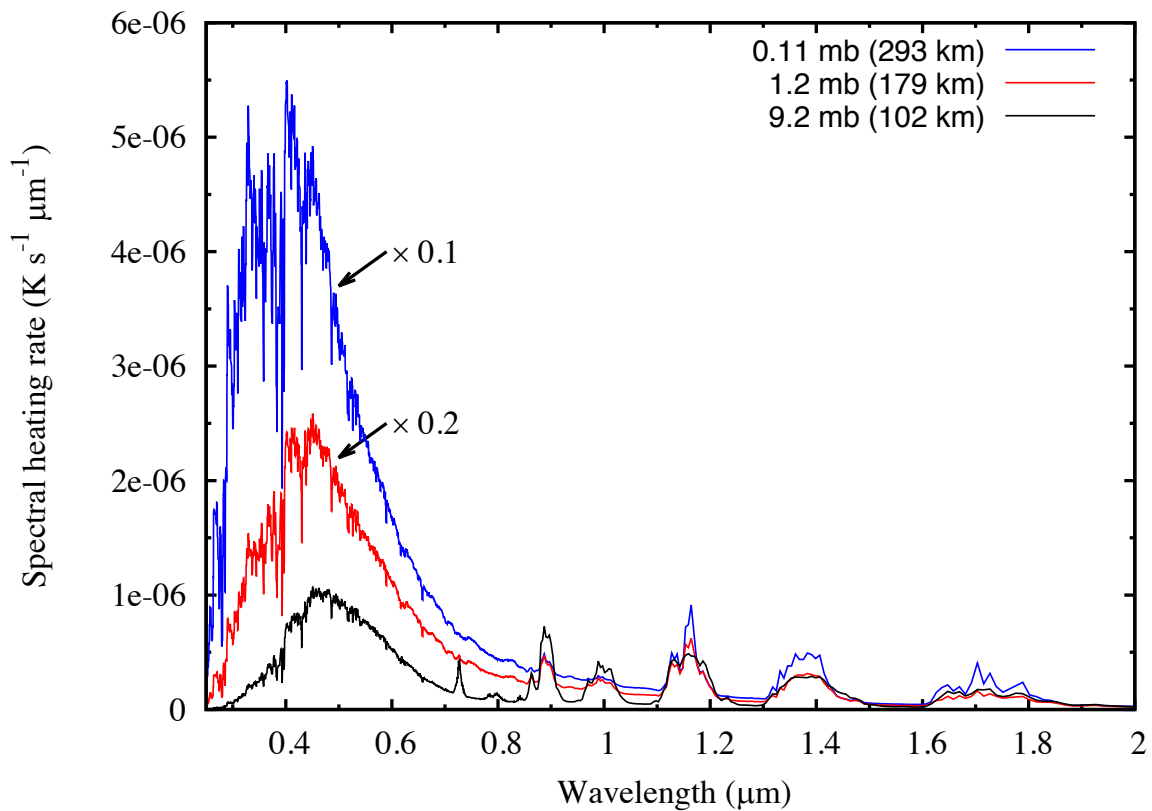
369

## 370 **4. Results**

371

### 372 *4.1 Heating and cooling rates in the stratosphere*

373 Figure 3 shows, at three different pressure levels, the spectral heating rate  $h_\lambda$ , giving the  
 374 wavelength dependence of the absorbed solar energy (the solar heating rate in Eq. 1 is  
 375  $h = \int h_\lambda d\lambda$ ). At pressures less than  $\sim 5$  mbar, heating is dominated by aerosol absorption of  
 376 solar radiation at wavelengths below  $0.8 \mu\text{m}$ , with a peak around  $0.4 \mu\text{m}$  at  $0.1$  mbar and  $0.45$   
 377  $\mu\text{m}$  at  $1$  mbar. At  $10$  mbar, the strong methane bands between  $0.8$  and  $3.7 \mu\text{m}$  provide  
 378 substantial additional heating. In this region, methane and aerosol absorption provide  
 379 comparable contributions to the solar heating while, at deeper levels, methane absorption  
 380 dominates.

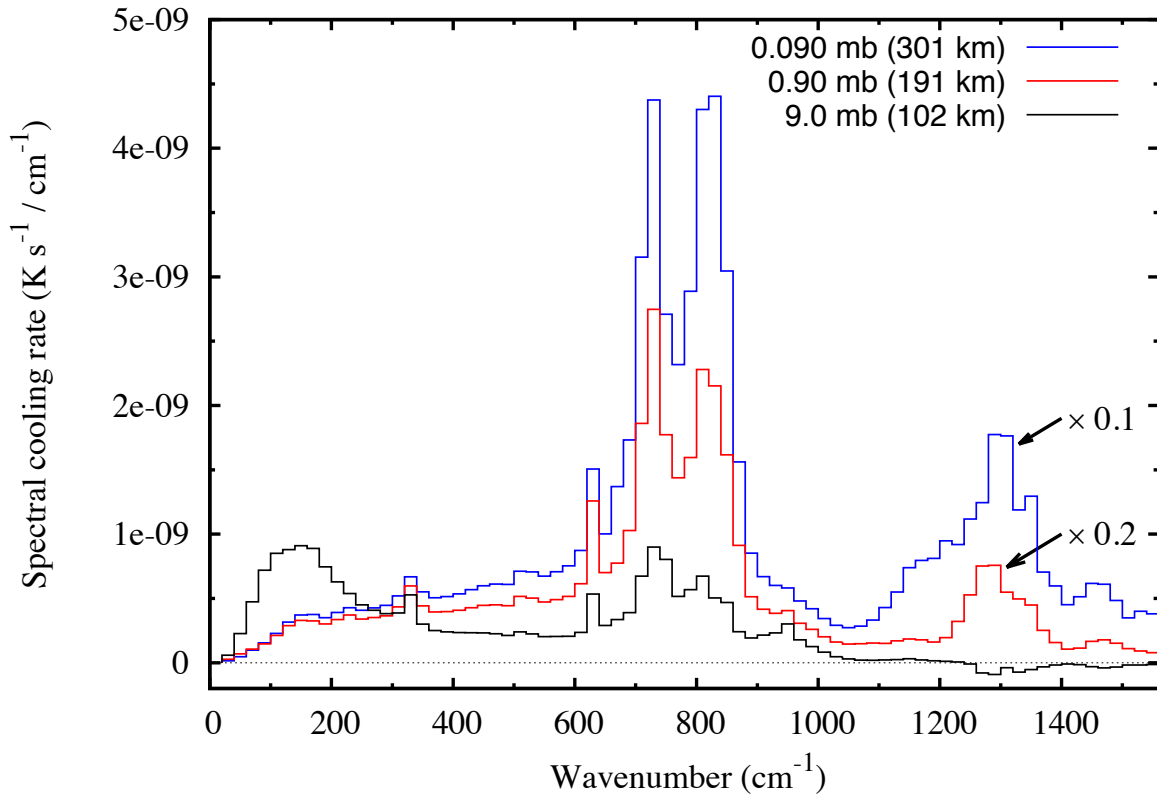


381

**Figure 3:** Spectral heating rate  $h_\lambda$  giving, as a function of wavelength, the contribution per unit wavelength to the day-averaged solar heating rate at three different atmospheric levels. For clarity,  $h_\lambda$  at  $0.11$  mbar is multiplied by  $0.1$  and  $h_\lambda$  at  $1.2$  mbar by  $0.2$ . The solar heating rate is integrated from  $0.25$  to  $3.8 \mu\text{m}$ . Insolation conditions correspond to  $20^\circ\text{S}$  and March 2007.

382

383



384

Figure 4: Spectral distribution of the cooling rate  $c_\sigma$ , averaged over  $20\text{-cm}^{-1}$  bins, giving, as a function of wavenumber, the contribution to the radiative cooling rate at three different atmospheric levels. For clarity,  $c_\sigma$  at 0.09 mbar is multiplied by 0.1 and  $c_\sigma$  at 0.9 mbar by 0.2. The temperature profile pertains to  $20^\circ\text{S}$  and March 2007.

385

386 The spectral distribution of the radiative cooling rate ( $c_\sigma$ ), averaged over  $20\text{-cm}^{-1}$  intervals, is

387 shown in Fig. 4 at three different levels in the stratosphere. The cooling rate  $c$  in Eq. 1 is the

388 integral over wavenumber of  $c_\sigma$ :  $c = \int c_\sigma d\sigma$ . The most efficient gaseous coolers are ethane

389 ( $820\text{ cm}^{-1}$ ), acetylene ( $730\text{ cm}^{-1}$ ) and, above the  $\sim 5$  mbar level, methane ( $1300\text{ cm}^{-1}$ ). Note

390 that at (and below) the 9-mbar level, the methane band heats the atmosphere from above.

391 Substantial cooling in the stratosphere arises from the continuous aerosol opacity. As noted

392 earlier by Tomasko et al. (2008b), the cooling effects of gas and aerosol emission are of the

393 same order. Note, in the 9-mbar cooling rate spectrum, the contribution from the nitrile haze

394 peaking at  $160\text{ cm}^{-1}$  (Anderson and Samuelson 2011).

395

396 In Fig. 5, we show the heating and cooling rate profiles calculated with our model for the  
397 composition and temperature profile derived from CIRS measurements near 20°S in March  
398 2007. Both profiles steadily decrease with depth, by more than 3 orders of magnitude from  
399 the lower mesosphere to the lower troposphere. In the whole region 0.1-5 mbar, best  
400 constrained by CIRS measurements in terms of temperature, haze and composition, the  
401 heating and cooling rate profiles are remarkably similar, the former being regularly 20-35%  
402 larger than the latter. The difference between them varies between  $3 \times 10^{-6} \text{ K s}^{-1}$  at 0.1 mbar  
403 and  $2 \times 10^{-7} \text{ K s}^{-1}$  at 5 mbar. As the observed temperature variation around 2007 is less than 1  
404  $\text{K year}^{-1}$  (Fig. 1), i.e.  $< 3 \times 10^{-8} \text{ K s}^{-1}$ , the energy balance equation (Eq. 1) implies that this  
405 difference has to be balanced by adiabatic cooling. This leads to upward velocities decreasing  
406 from  $0.25 \text{ cm s}^{-1}$  at 0.1 mbar to  $0.09 \text{ cm s}^{-1}$  at 1 mbar and  $0.014 \text{ cm s}^{-1}$  at 5 mbar.

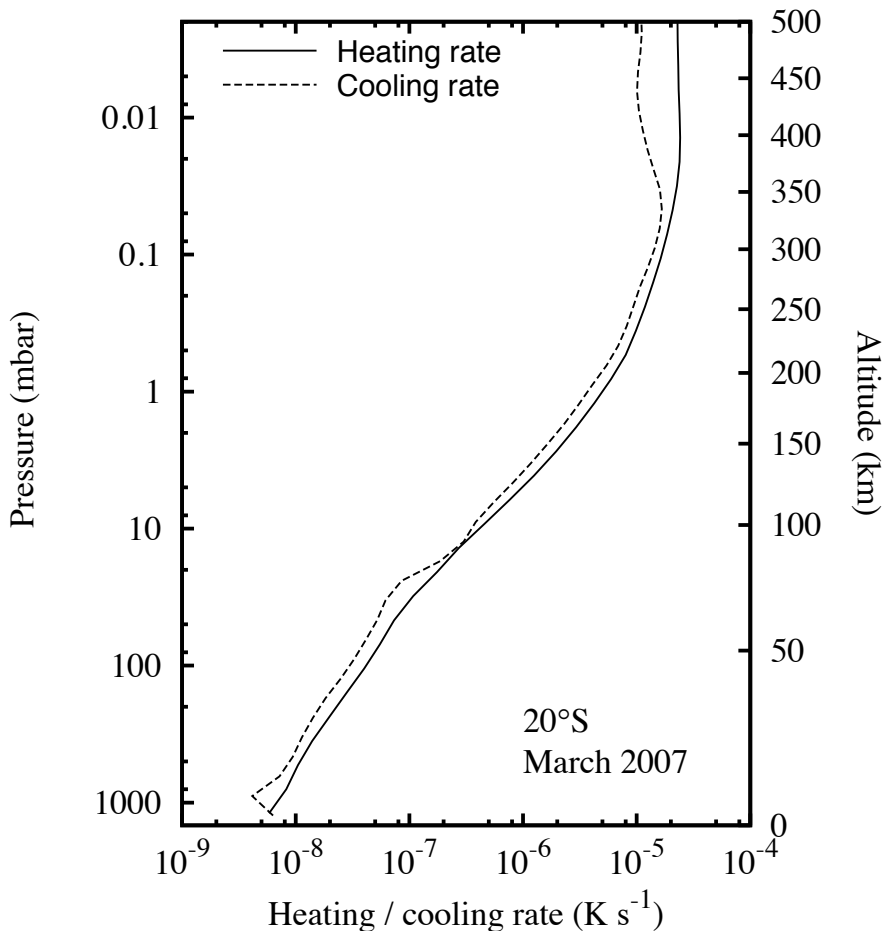


**Figure 5:** Heating (solid line) and cooling (dashed line) rate profiles calculated with our model using the temperature profile retrieved from CIRS measurements at 20°S in March 2007. The heating rate profile corresponds to day-averaged conditions and insolation parameters for March 2007.

407

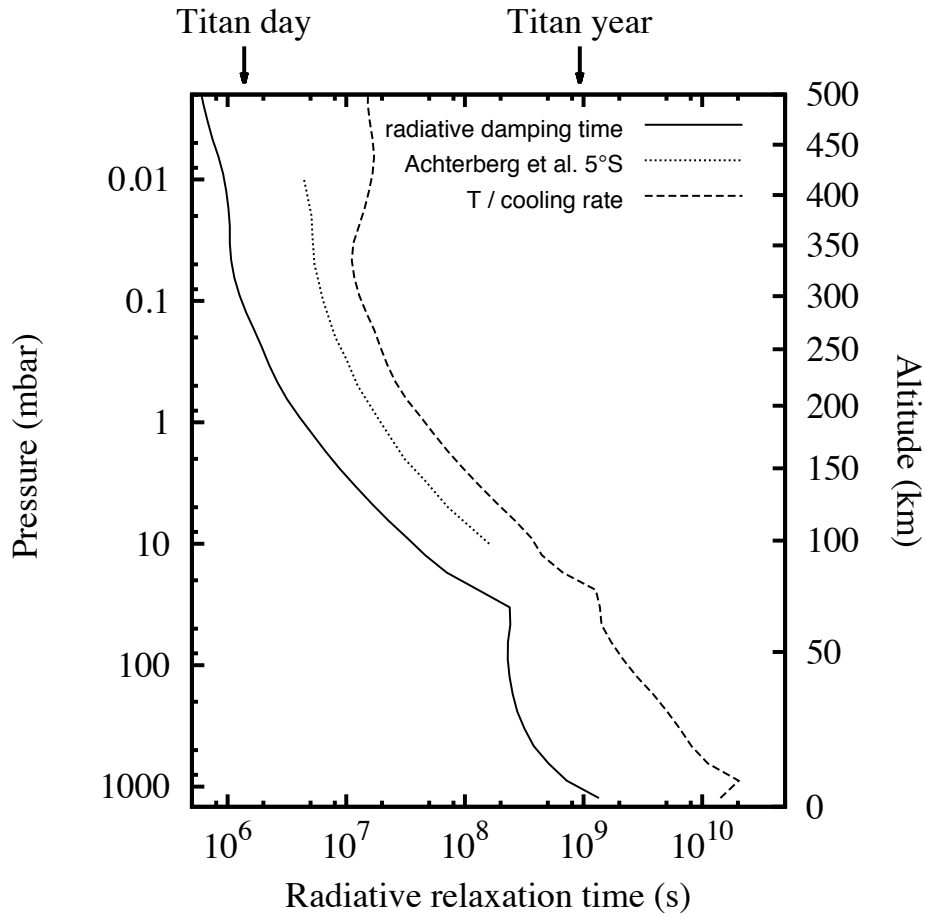
408 Around 15 mbar (85 km), which corresponds to the peak of the nitrile haze, the cooling and  
409 heating rates are almost equal. Just below, around 25 mbar (71 km), the heating rate exceeds  
410 the cooling rate by about 70%. This region corresponds to the fall-off of the C<sub>2</sub>H<sub>6</sub> and C<sub>2</sub>H<sub>2</sub>  
411 mixing ratios due to condensation, these two gases being important infrared radiators in the  
412 whole stratosphere. Below the 50-mbar level, in the troposphere, the heating rate is about  
413 40% larger than the cooling rate. Note that no information from CIRS data is available using  
414 the  $\nu_4$  CH<sub>4</sub> band below the  $\sim$  10-mbar level, and the temperature profile then joins the  
415 Huygens/HASI *in situ* measurements at 10°S (Fulchignoni et al. 2005). Above the  $\sim$  0.03-  
416 mbar level, the heating rate is about twice the cooling rate, which would call from Eq. 1 for an  
417 upward velocity  $w$  of about 1.5 cm s<sup>-1</sup>. However, this estimation is very uncertain due to the  
418 poorly known haze density in this region.

419

#### 420 *4.2 Radiative relaxation times*

421 Evaluation of radiative time constants is important to investigate the response of Titan's  
422 atmosphere to various perturbations, such as the diurnal and seasonal cycles of insolation, or  
423 atmospheric waves. As discussed by Flasar et al. (2014), the radiative time constant ( $\tau_r$ ) is the  
424 characteristic time for radiatively damping out a small perturbation from the equilibrium state,  
425 keeping unchanged all other energy terms such as solar and dynamical heating. From Eq. 1,  $\tau_r$   
426 is formally equal to the inverse of the derivative of the cooling rate with respect to  
427 temperature:

428  $\tau_r(z) = 1 / \frac{\partial c(z)}{\partial T(z)}$  (7)



429

Figure 6: Vertical profiles of radiative relaxation time in Titan's atmosphere. The solid line corresponds to damping out a Gaussian temperature perturbation having a full width at half maximum of one pressure scale height. The dotted line shows the radiative time constant calculated by Achterberg et al. (2011) at 5°S using the direct cooling-to-space approximation for the radiative cooling. The dashed line represents the temperature divided by the cooling rate, following the approach of Strobel et al. (2009).

430

431 However,  $c(z)$  in a given layer depends to some extent, through exchange terms, on the  
 432 temperature outside this layer so that the vertical shape of the assumed perturbation has to be  
 433 specified. We assumed here a Gaussian perturbation having a FWHM of 1 pressure scale

434 height and centered in a layer  $[p_i; p_{i+1}]$ . Doing so,  $\frac{\partial c(z)}{\partial T(z)}$  can be calculated from Eq. 5 as a

435 linear combination of terms in the form  $(A_{i+1,j,k} - A_{i,j,k}) \frac{\partial B_{\sigma_k} [T(p_j)]}{\partial T(p_j)}$  where  $j$  runs over the  
436 perturbed levels with appropriate weighting. The resulting profile of  $\tau_r$  is shown in Fig. 6 as a  
437 solid line.

438

439 The radiative time constant readily increases with depth from less than 1 Titan day above the  
440 0.1-mbar level to about 1 Titan year in the lowest layers of the troposphere. In the range 0.1-5  
441 mbar, in which we are mostly interested here, the radiative time constant varies between  
442 0.0015 and 0.02 Titan year, implying that the stratosphere can respond radiatively to the  
443 seasonally-varying insolation with negligible time lag. We also made a calculation for a  
444 perturbation having a twice larger FWHM (2 scale heights). The resulting time constants are  
445 then  $\sim 25\%$  larger in the stratosphere and  $\sim 60\%$  in the troposphere below the 300-mbar level.

446

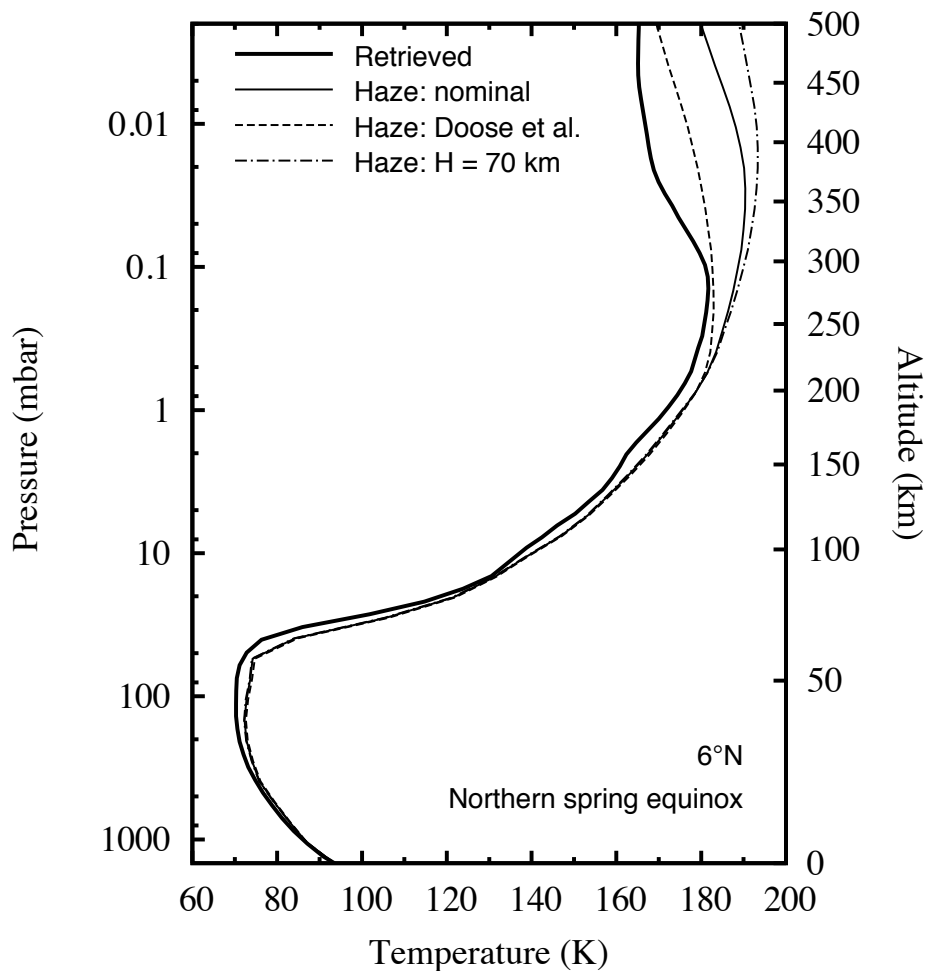
447 In Fig. 6, we also show the radiative cooling timescale calculated by Achterberg et al. (2011)  
448 at  $5^\circ\text{S}$  using the direct cooling-to-space approximation and including opacity from  $\text{CH}_4$ ,  $\text{C}_2\text{H}_2$   
449 and  $\text{C}_2\text{H}_6$ . Their time constants are 4-5 times larger than those inferred in this work. A factor  
450 of  $\sim 2$  is likely due to the lack of aerosols and other gases in their calculations and the  
451 remaining difference from ignoring the exchange terms, as discussed in Section 5. We also  
452 plotted in Fig. 6, the ratio of temperature to cooling rate ( $T(z)/c(z)$ ), which yields a simpler  
453 estimate of the radiative timescale. As can be seen from Eq. 1, rather than relevant to damping  
454 of a temperature perturbation, this time constant pertains to a case in which the solar heating  
455 is turned off (as well as the dynamical term). This is the approach that was used by Strobel et  
456 al. (2009) to compute the radiative timescale. Figure 6 shows that, doing so, the radiative  
457 damping time is overestimated typically by a factor of 10.

458



459 4.3 Temperature profile at 6°N

460 We first compare the predictions of our seasonal radiative model, with no adiabatic  
461 heating/cooling, to the temperature profile retrieved near 6°N around northern spring equinox  
462 (See Section 2), a region where seasonal variations of insolation are minimal. Figure 7 shows  
463 the temperature profile calculated with the three haze profiles of Fig. 2. Temperatures in these  
464 models essentially differ above 200 km due to different assumptions on the vertical profile of  
465 aerosol extinction. The warmest profile is associated with the largest aerosol number  
466 extinction profile and vice versa, confirming that aerosol heating from scattering and  
467 absorption of solar radiation dominates over their cooling effect due to thermal emission. The  
468 difference between the extreme profiles increases from 7 K at 0.1 mbar to 20 K at 0.001 mbar.

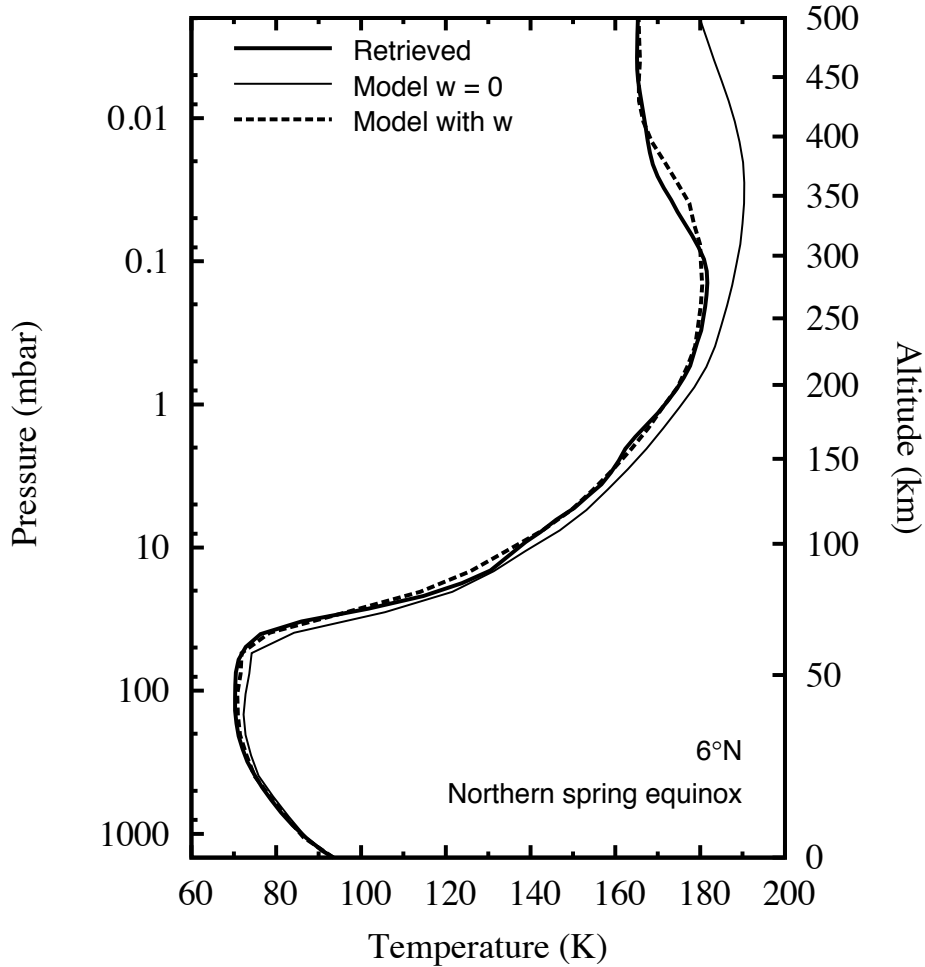


469

**Figure 7:** Comparison of a temperature profile retrieved from Cassini/CIRS measurements around 6°N and northern spring equinox (thick solid line) with radiative model profiles calculated for the three haze models in Fig. 2. No dynamical term is included in the energy equation.

470

471 Whatever haze profile is used, the radiative model profile is warmer than the retrieved one at  
472 all levels except around 15 mbar (85 km). Note that below 5 mbar, the profile is not  
473 constrained by Cassini/CIRS measurements but essentially represents the Huygens/HASI  
474 profile (10°S, January 2005). To bring the calculated and observed profiles closer, it is  
475 necessary to add adiabatic cooling. For our nominal haze model, we find that a constant  
476 vertical velocity, expressed in pressure coordinates ( $\frac{dP}{dt} = -\rho g w$ , where  $\rho$  is the atmospheric  
477 density), of  $\approx -1.3$  Pa per Titan day up to the 0.6-mbar level, slightly decreasing in amplitude  
478 at higher altitudes to reach  $\approx -1.0$  Pa per Titan at 0.02 mbar, allows us to reproduce fairly well  
479 the observed profile from the 0.05-mbar level down to the troposphere (Fig. 8, dashed line).  
480 The largest discrepancy occurs around 15 mbar, where the model profile is 5 K colder than  
481 the Huygens profile.



482

Figure 8: Comparison of a temperature profile retrieved from Cassini/CIRS measurements around 6°N and northern spring equinox (thick solid line) with two radiative model profiles using the nominal haze model. The thin solid line shows the case with no additional adiabatic heating (same as in Fig. 7). The dashed line shows a model with a constant velocity below the 0.6-mbar level, when expressed in pressure coordinates, equal to -1.3 Pa / Titan day, decreasing to -1.0 Pa / Titan day at 0.02 mbar and -0.5 Pa / Titan day at 0.01 mbar (Fig. 9).

483

484

This velocity profile corresponds to an upward vertical velocity  $w$  in the range 0.03-0.05 cm

485

$s^{-1}$  at 1 mbar, taking into account a 1 K uncertainty (Fig. 9), which corresponds to the

486

dispersion in our 6°N temperature profile selection (Section 2).  $w$  varies as  $(\rho g)^{-1}$  below the

487

0.6-mbar level and as  $(\rho g)^{-0.92}$  in the 0.6-0.02 mbar range. At higher levels, the velocity is set

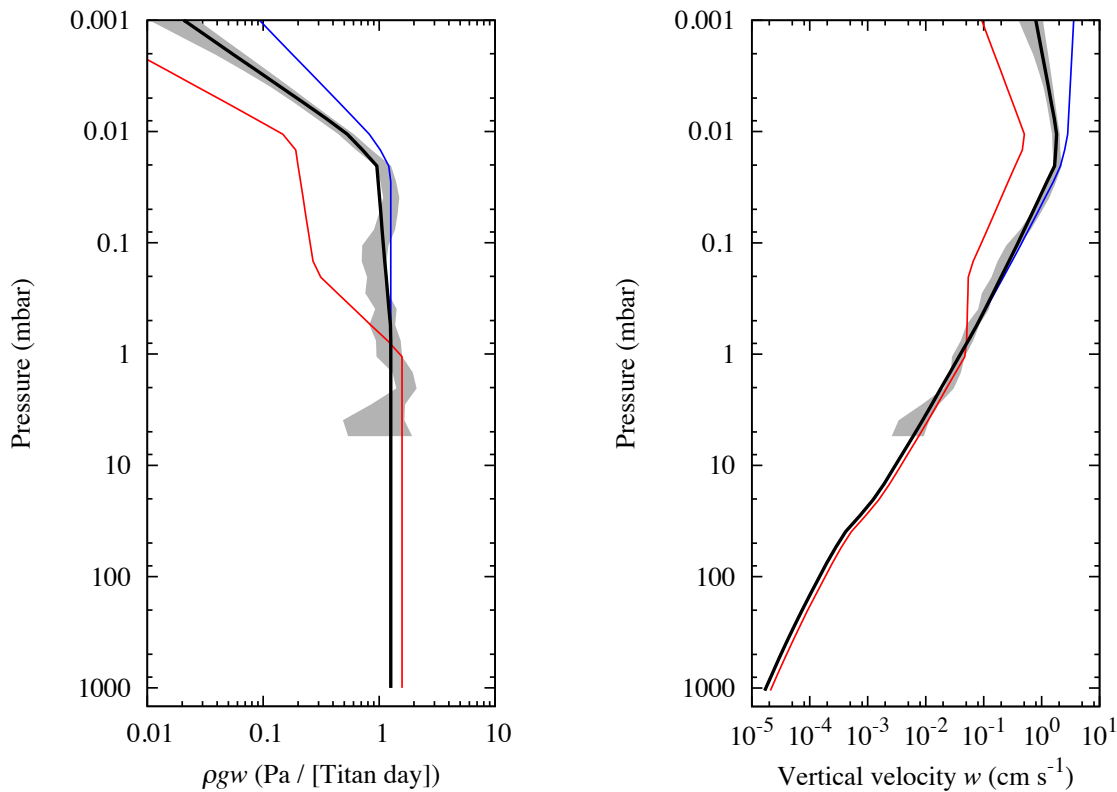
488

so that it varies as  $(\rho g)^{-0.1}$  from 0.02 to 0.01 mbar, and as  $(\rho g)^{0.35}$  above (Fig. 9). The

489

approximate constancy of  $\frac{dP}{dt}$  below the 0.02-mbar level suggests only weak divergence of

490 the upward flow in the stratosphere, while the decrease of  $\frac{dP}{dt}$  at higher levels implies stronger  
 491 divergence, i.e. horizontal poleward motion. However, this conclusion is not firm due  
 492 uncertainties in the haze profile. It still holds if we use the upper limit for the haze density (“H  
 493 = 70 km” case) but not for the lower limit (Doose et al. profile), in which case a strong  
 494 decrease of  $\frac{dP}{dt}$  above the  $\approx 1$  mbar level is required to reproduce the 6°N temperature profile  
 495 (Fig. 9).



496

**Figure 9:** Upward velocity profile used to model the temperature profile retrieved at 6°N around equinox, given in pressure units per Titan day (left panel) and in  $\text{cm s}^{-1}$  (right panel). The black line corresponds to the model with the nominal haze profile that yields the best fit of the temperature profile (Fig. 8), while the red line corresponds to the Doose et al. profile and the blue line to the “H = 70 km” haze profile shown in Fig. 2. The grey area around the best fit velocity profile corresponds to a temperature uncertainty taken as the standard deviation of our 6°N temperature profile selection given in Section 2.

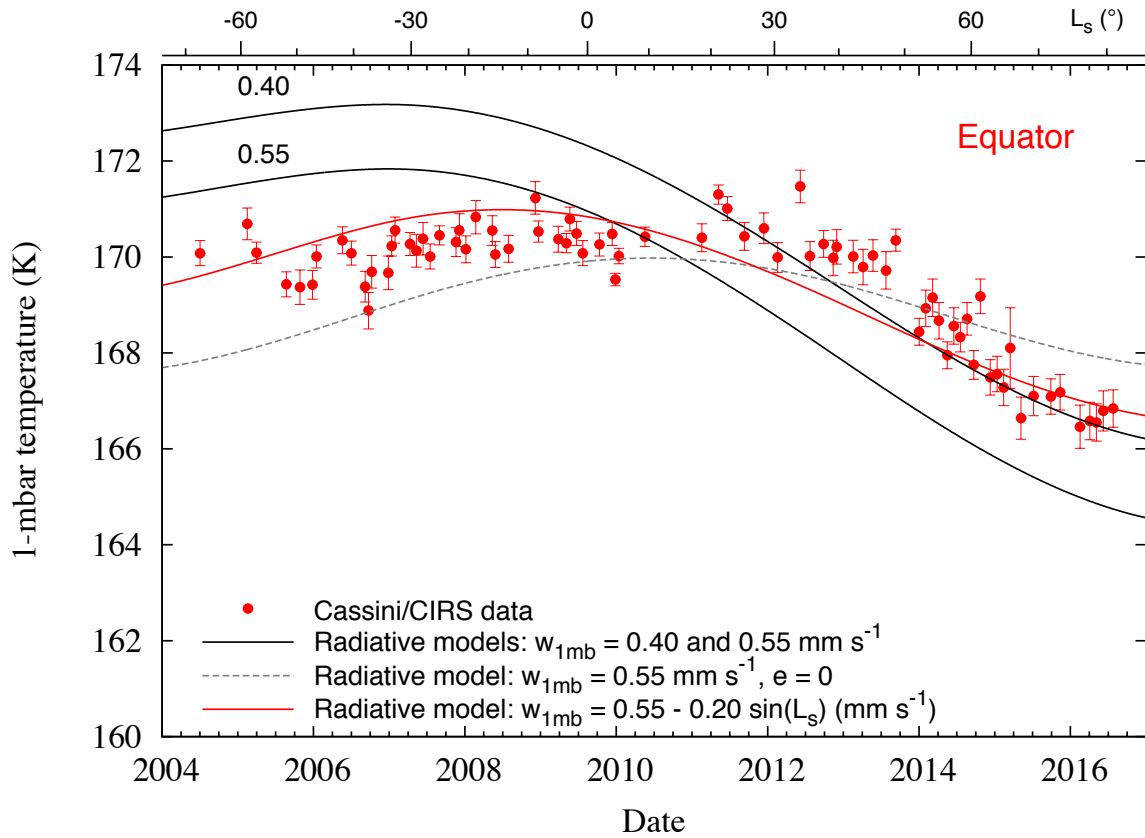
497

498 *4.4 Seasonal variations of temperature at 1 mbar*

499 We first investigate here the variations of temperatures at 1 mbar derived from Cassini/CIRS  
 500 in the equatorial region from 2004 to 2016 (Fig. 1). Figure 10 shows our model predictions  
 501 using a constant upward velocity of  $0.040 \text{ cm s}^{-1}$  at 1 mbar as derived above around  $6^\circ\text{N}$  near  
 502 northern spring equinox. This model predicts a  $\sim 7 \text{ K}$  drop between pre-equinox (2006-2008)  
 503 and 2016. This variation is due to Saturn's eccentricity of 0.054, which modulates the  
 504 distance to the Sun and thus the solar flux striking the Saturn system. A model with zero  
 505 eccentricity (dashed line in Fig. 10) shows a shallow maximum around mid 2010 and similar  
 506 temperatures in 2006 and 2016. In contrast, the model accounting for the orbital eccentricity  
 507 predicts a maximum around 2007, between the perihelion (July 2003) and the equinox  
 508 (August 2009), followed by a decrease due to the increasing distance with the Sun. In fact,  
 509 while the temperatures after 2012 are then correctly reproduced by this model, the contrast  
 510 between pre-equinox and 2016 ( $\sim 7 \text{ K}$ ) is even larger than the observed value of  $\sim 4 \text{ K}$ .  
 511 Increasing the vertical velocity in the model uniformly shifts the calculated temperatures and  
 512 does not help to reduce the contrast (Fig. 10). To better reproduce the observations, a  
 513 modulation of the vertical velocity, i.e. of the adiabatic cooling, is required. We chose to do  
 514 so by simply adding a sine function of the heliocentric longitude  $L_s$  to the velocity, which then  
 515 becomes:

$$516 \quad w(p) = w_c(p) + w_m(p) \sin L_s \quad (8)$$

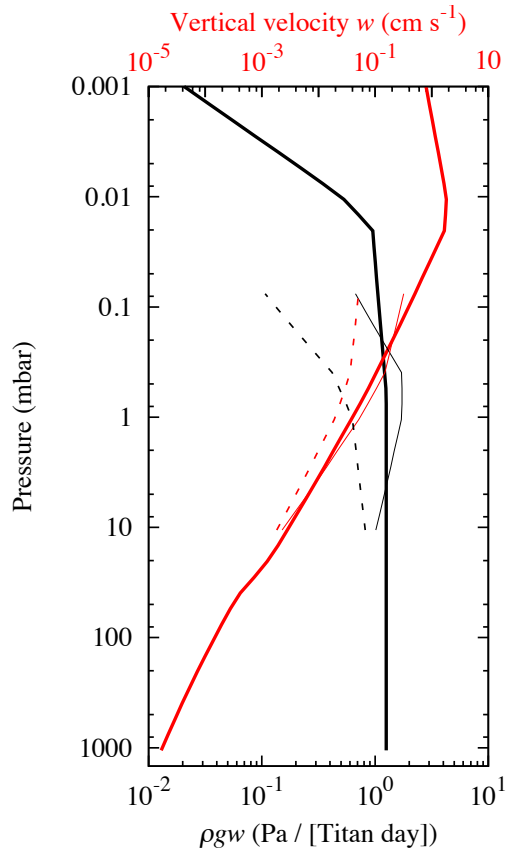
517 At the 1-mbar level,  $w_c = 0.055 \text{ cm s}^{-1}$  and  $w_m = 0.020 \text{ cm s}^{-1}$  allows us to reproduce relatively  
 518 well the observed variation (red line in Fig. 10). The vertical velocity at 1 mbar then varies  
 519 seasonally between  $0.035$  and  $0.075 \text{ cm s}^{-1}$  but is always positive (upward), meaning  
 520 dynamical cooling of the equatorial region all year through. Note that the vertical profile of  $w_c$   
 521 used here and shown in Fig. 11 differs somewhat from those used at  $6^\circ\text{N}$  in Section 4.3  
 522 because it was adjusted to better match the temperatures at 0.2, 0.5, 1, 2 and 4 mbar retrieved  
 523 by Achterberg et al. (in preparation) and shown in Section 4.6.



524

Figure 10: Time variation of 1-mbar temperatures in the equatorial region are compared with predictions from our seasonal radiative model. Solid lines represent models with constant-with-time upward velocity profiles having  $w(1 \text{ mbar}) = 0.040$  and  $0.055 \text{ cm s}^{-1}$ . The dashed line represents a model with  $w = 0.055 \text{ cm s}^{-1}$  and the orbital eccentricity set to zero. The red line represents a model with a seasonally-varying vertical velocity profile:  $w(1 \text{ mbar}) = 0.055 - 0.020 \sin(L_s) \text{ cm s}^{-1}$ , where  $L_s$  is the heliocentric longitude.

525



526

**Figure 11:** Thick solid lines: upward velocity profile used to model the temperature profile retrieved at 6°N around equinox (Fig. 8), given in pressure units per Titan day (black) and in cm s-1 (red). Thin solid lines: year-averaged upward velocity profile  $w_c$  used to model the seasonal temperature variations at the equator as retrieved by CIRS (Figs. 10 and 15). Thin dashed lines: amplitude of the sine term of this upward velocity profile  $w_m$ . See Eq. 8. Note that  $w_c$  and  $w_m$  are constrained from CIRS observations only from 0.2 to 4 mbar.

527

528 We then applied our model to latitudes 30°N and S where seasonal variations of insolation are  
 529 more pronounced. Figure 12 shows the predicted variations of temperature at 1 mbar over a  
 530 full Saturnian year (29.46 years), using a constant-with-time upward velocity profile (with  
 531  $w = 0.055 \text{ cm s}^{-1}$  at 1 mbar). Such a model predicts large variations of temperature as a  
 532 response to the seasonally-varying insolation with peak-to-peak amplitudes of 33 K at 30°S  
 533 and 19 K at 30°N. The amplitudes are stronger in the southern hemisphere than in the  
 534 northern due to the orbital eccentricity, the perihelion occurring less than a year before  
 535 southern summer solstice. Clearly, the predicted variations are much stronger than observed

536 by Cassini since 2004 (Fig. 12). Most noticeable in this comparison is the observed decrease  
537 of the 1-mbar temperature since 2013 at 30°N, which is at odds with the increase predicted by  
538 the radiative model as a result of increasing insolation. This behavior can only be explained  
539 by an increase of the dynamical cooling with time at this latitude. More generally, the  
540 observed variations at 30°N and S point to dynamics acting to counterbalance the seasonal  
541 variations in the solar heating. This means dynamical heating, or reduced cooling, in winter  
542 and enhanced dynamical cooling in summer. To model this pattern in a simple way, we  
543 proceeded as above and modulated the vertical velocity in the form of Eq. 8. The best fits to  
544 the data that we obtained are shown in Figs. 13-14 with the corresponding values of  $w_c$  and  
545  $w_m$  given in Table 1. As can be seen, this simple model is able to reproduce the observed  
546 variations relatively well.

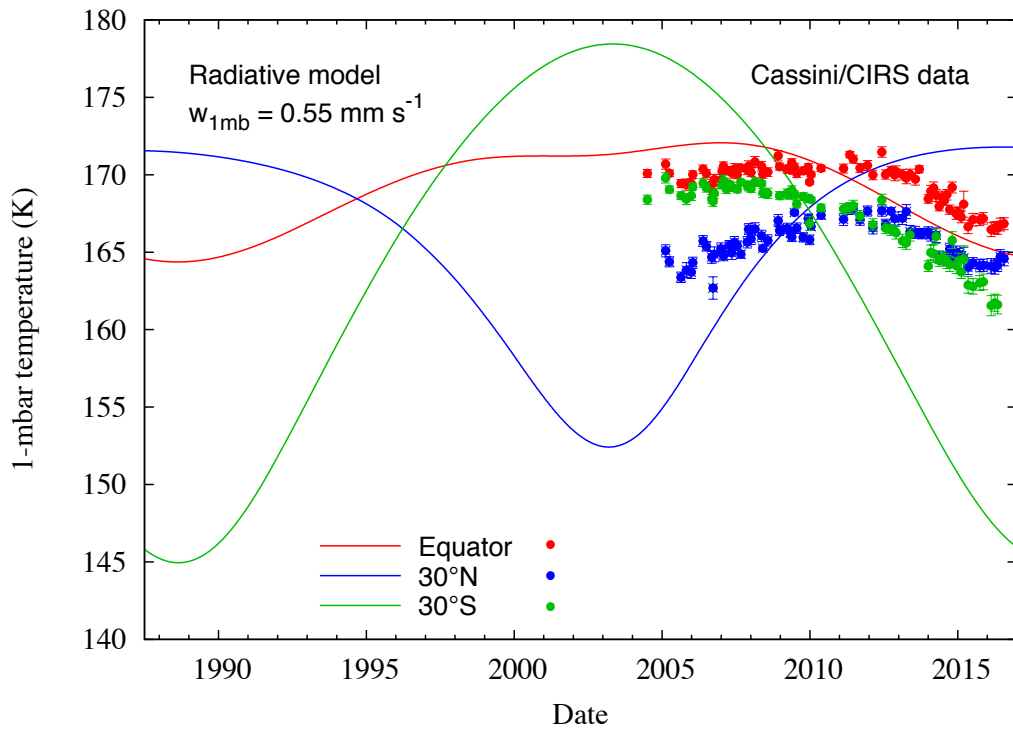
547

548 **Table 1.** Model parameters for the vertical velocity profile<sup>1</sup>

Latitude	$w_c$ (1 mbar) (cm s <sup>-1</sup> )	$w_m$ (1 mbar) (cm s <sup>-1</sup> )	Pressure range (mbar)	$\alpha_c$	$\alpha_m$
Equator	+0.055	-0.020	< 0.01	-0.40	-0.40
30°N	+0.063	+0.075	0.01-0.025	0.20	0.20
30°S	+0.053	-0.105	0.025-0.4	0.45	0.30
			0.4-1	1.0	0.60
			> 1	1.2	0.90

549 <sup>1</sup>: upward velocity is modeled as  $w(p) = w_c(p) + w_m(p) \sin L_s$ , and  $w_c$  (resp.  $w_m$ ) varies as  
550  $(\rho g)^{-\alpha_c}$  (resp.  $(\rho g)^{-\alpha_m}$ ) in a given pressure range.  
551

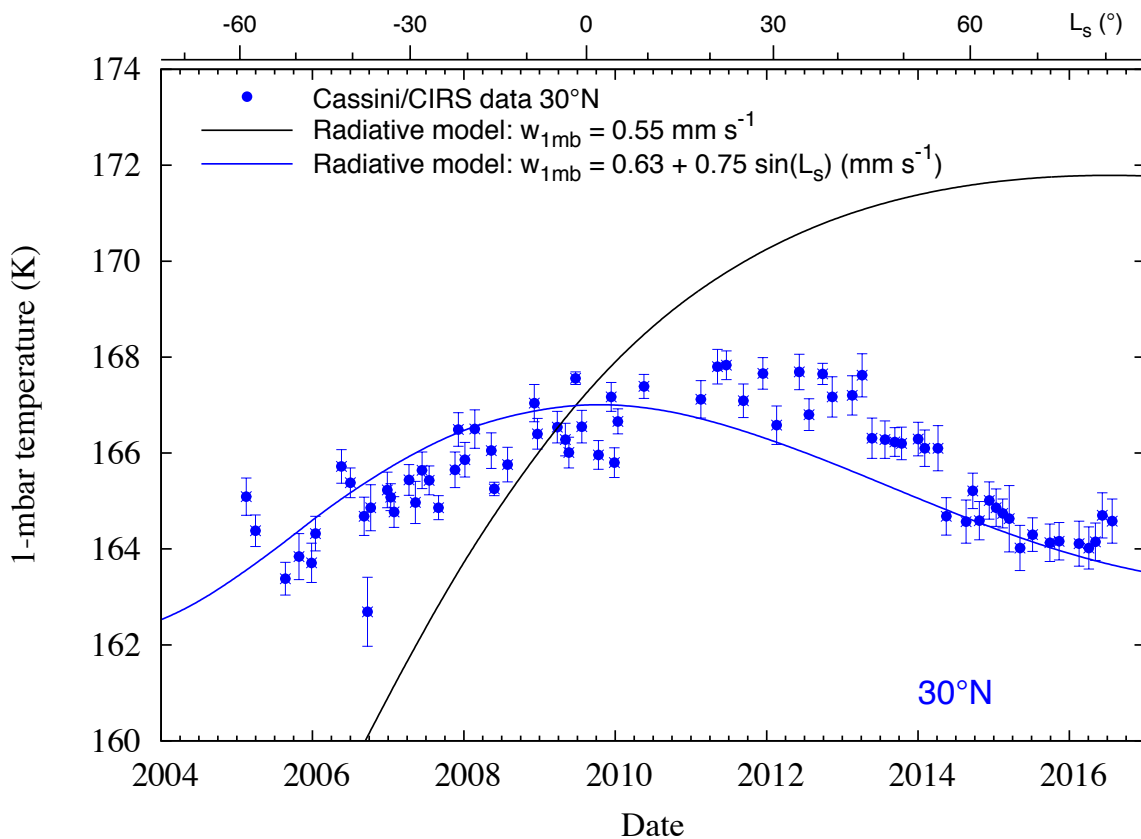




552

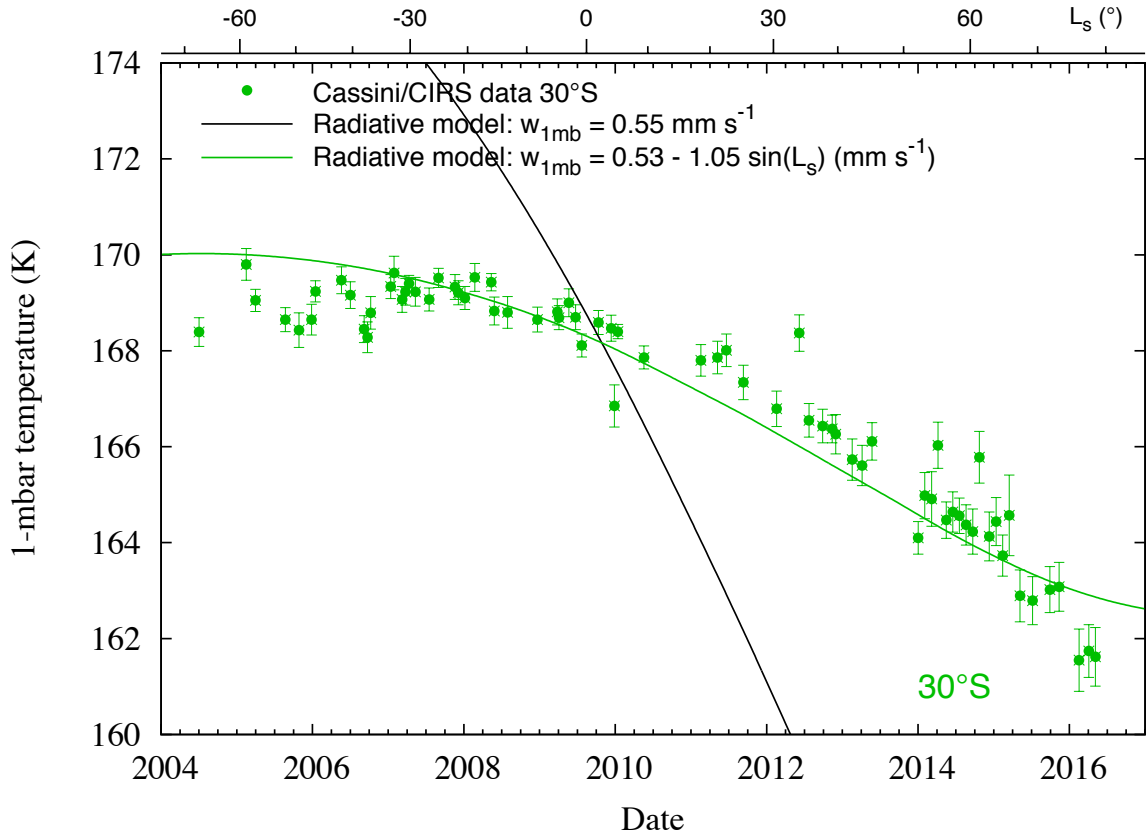
553 **Figure 12:** Time variation of 1-mbar temperatures at 0°, 30°N and 30°S predicted by the  
 554 seasonal radiative model using a constant-with-time upward velocity profile with  $w(1$   
 555 mbar) = 0.055 cm s<sup>-1</sup>. Data retrieved from Cassini/CIRS measurements (Fig. 1) are  
 overlotted for comparison.

555



556

557 **Figure 13:** Time variation of 1-mbar temperatures at 30°N predicted by the seasonal  
 558 radiative model are compared with data retrieved from Cassini/CIRS measurements (Fig.  
 559 1). Black line: constant-with-time vertical velocity; colored line: vertical velocity varying  
 with solar longitude (see parameters in Table 1).

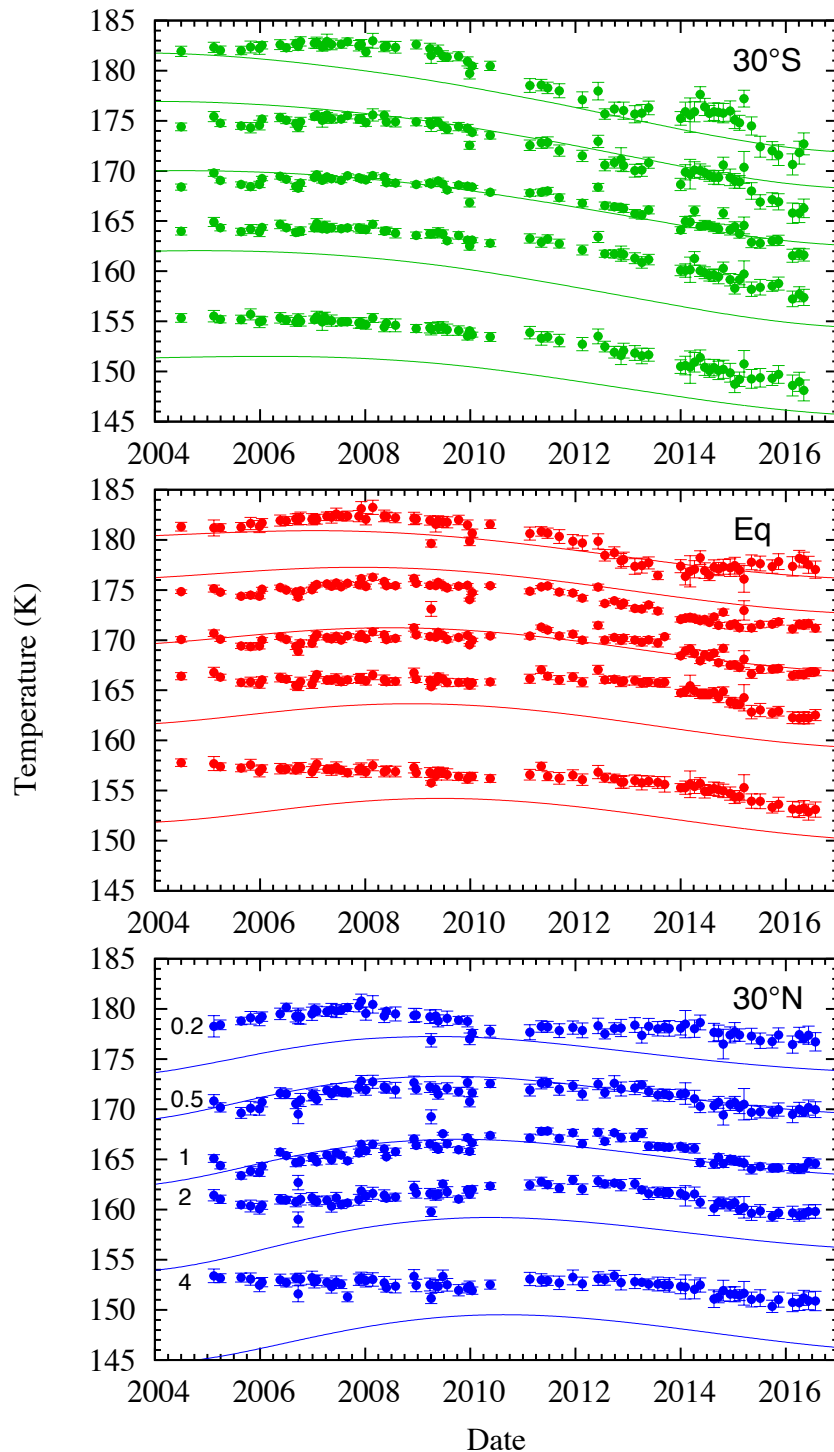


560 **Figure 14:** Same as Fig. 12 for 30°S.

562  
 563 *4.5 Seasonal variations of temperature at other levels*

564 In Section 4.4, we focused on the 1-mbar level, which is the region best constrained by  
 565 Cassini/CIRS observations in terms of haze properties and temperature, and we have tuned  
 566 our model to best reproduce the data at this level. In this section, we extend our modelling up  
 567 to 0.2 mbar and down to 4 mbar, where temperature information is also available (Fig. 15). To  
 568 do so, we used a vertical velocity profile  $w(p)$  varying as  $(\rho g)^{-\alpha}$  in a given pressure range as  
 569 indicated in Table 1 and shown in Fig. 9 at the equator. As we intend to keep a smooth  
 570 variation for  $w(p)$ , we did not try to match exactly the average temperature at a given pressure

571 level apart from that at 1 mbar. We then have typical discrepancies of  $\pm 3$  K on the average  
572 temperatures which may be due to uncertainties in our haze model above  $\sim 0.4$  mbar (Fig. 7)  
573 and possibly systematic uncertainties in the temperature retrievals below  $\sim 2$  mbar. We are  
574 therefore more interested here in the seasonal variations of temperature at a given level than  
575 in their absolute mean values.



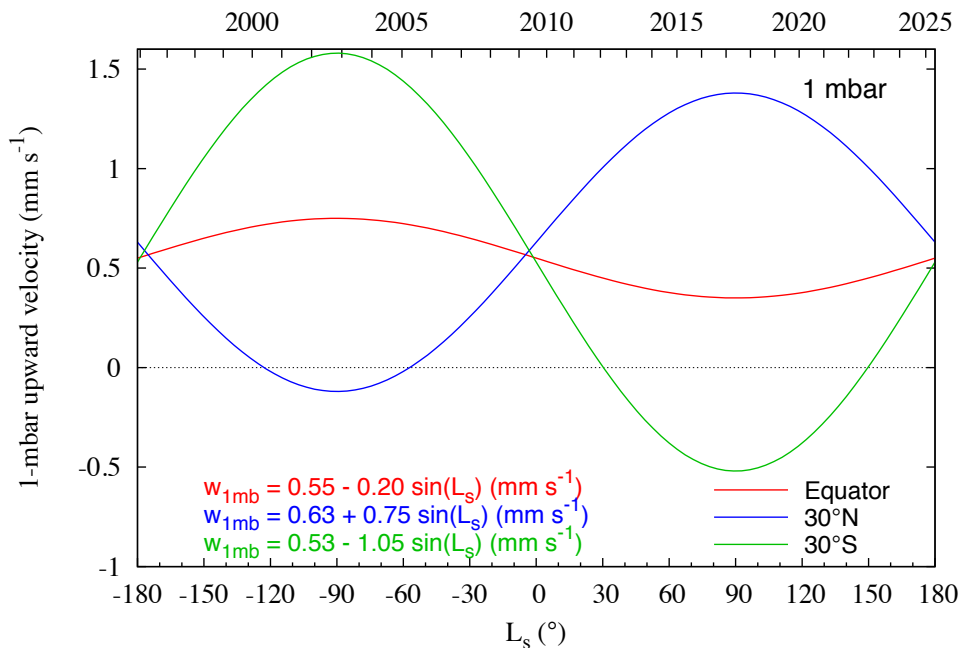
576

577  
578  
579

**Figure 15:** Time variation of temperatures at 0.2, 0.5, 1, 2 and 4 mbar predicted by the seasonal radiative model (colored lines) are compared with data retrieved from Cassini/CIRS measurements at 30°S, equator and 30°N. In this model, the vertical velocity varies as an affine function of  $\sin L_s$  (see parameters in Table 1).

580

581 In Fig. 15, we show the seasonal variations of temperature predicted by our model for  
582 different pressure levels at 0, 30°N and 30°S. In these “best-fit” models, the vertical variation  
583 of the constant and sine components of the velocity profile were chosen to reproduce  
584 satisfactorily the observed seasonal variations at the three latitudes simultaneously (only one  
585 set of parameters for all latitudes, given in Table 1). On the other hand, the velocity terms  $w_c$   
586 and  $w_m$  at 1 mbar were adjusted at each latitude to best reproduce the seasonal variations at  
587 this level, as discussed in Section 4.4. The CIRS-derived variations are overall fairly well  
588 reproduced except noticeably at 4 mbar where the steady decrease of temperature at the  
589 equator and at 30°N before equinox (2009) is not predicted by the model.



590  
591  
592

**Figure 16:** Time variation of the 1-mbar model upward velocity at 0°, 30°N and 30°S as a function of heliocentric longitude (lower scale) and year (upper scale).

593 The seasonal variation of the model velocity profile  $w$  at 1 mbar is shown in Fig. 16 for the  
594 three latitudes. The seasonal variation at other pressure levels can be obtained from the  
595 parameters in Table 1. The vertical dependence of the two components ( $w_c$  and  $w_m$  in Eq. 8) is  
596 illustrated in Fig. 11.

597

## 598 **5. Discussion**

599

### 600 *5.1 Heating and cooling rates*

601 Tomasko et al. (2008b) computed the solar heating rate at Huygens probe-landing latitude,  
602 averaged over longitude, using the haze model derived from DISR measurements by  
603 Tomasko et al. (2008c) and methane absorption coefficients simultaneously derived from  
604 DISR measurements (Tomasko et al. 2008a). The solar heating rates we derived at 20°S in  
605 March 2007 do not differ from those of Tomasko et al. by more than  $\pm 25\%$  in the range 10-  
606 170 km. The largest differences occur at 10 and 170 km where our heating rate is some 20%  
607 larger and near 90 km where our heating rate is 25% smaller. We regard these differences as  
608 acceptable given the difference in the haze model, which was recently updated by Doose et al.  
609 (2016), and in the methane absorption, which we calculate using the ab initio TheoReTS  
610 database (Rey et al. 2017).

611

612 Cooling rates corresponding to the temperature, gas and haze profiles derived from Huygens  
613 and Cassini/CIRS data were also calculated by Tomasko et al. (2008b). Our cooling rate  
614 profile agree with theirs to within  $\pm 20\%$  in the whole altitude range 10-400 km, with the  
615 maximum discrepancy occurring near 10 km (ours is 20% smaller) and 70 km (ours is 20%  
616 larger).

617

618 Comparing the heating and cooling rates calculated at the Huygens landing site, Tomasko et  
619 al. (2008b) concluded that the former exceeds the latter by a maximum of 0.5 K per Titan day  
620 near 120-130 km and that the excess decreases strongly below and above this altitude. At 125  
621 km, we derive 0.4 K / Titan day, in good agreement with Tomasko et al. Below this altitude,  
622 we also find that the net radiative heating minus cooling rate decreases rapidly, e.g. 0.07 K /  
623 Titan day at 70 km and 0.02 K / Titan day at 50 km, quite similar to Tomasko et al.'s results.  
624 On the other hand, we do not infer any decrease of this net radiative heating minus cooling  
625 above 120-130 km, but instead a regular increase up to 3 to 4 K per Titan day at 250-300 km.  
626 We note however that the decrease at higher altitudes invoked by Tomasko et al. is very  
627 uncertain given the large uncertainties in their haze model above 140 km, the altitude where  
628 the Huygens probe began measurements. Our haze model is also uncertain above ~200 km,  
629 where the net radiative heating minus cooling rate reaches ~2 K per Titan day.

630

631 We can also compare our calculations with the General Circulation Model (GCM) of  
632 Lebonnois et al. (2012, Fig. 10). At 20°S, their annual average of the solar heating rate is  
633 almost twice as large as ours at 90-100 km, 50% larger at 60 km and 30% larger at 50 km.  
634 These differences likely originate from differences in the haze model, that in Lebonnois et  
635 al.'s GCM being coupled with the 3-dimensional circulation and not imposed from  
636 observational constraints. More significant for our model comparison may be the ratio of  
637 dynamical cooling to total (radiative plus dynamical) cooling, also equal to radiative solar  
638 heating on an annual average basis. At 6°N, where seasonal modulation is minimum, this ratio  
639 can be determined from Fig. 10 of Lebonnois et al. at 85 and 66 km as approximately 18%  
640 and 25% respectively. Using the vertical velocity of 1.1 Pa / Titan day that we inferred in  
641 Section 4.3 at this latitude and the yearly-averaged solar heating rate from our model, we  
642 obtain ratios of 17% at 85 km and 28% at 66 km, in excellent agreement with Lebonnois et

643 al.'s GCM outputs. Lebonnois et al. (2012) do not provide information to compare results  
644 above 100 km.

645

## 646 *5.2 Radiative relaxation times*

647 In Section 4.2, we calculated the radiative time constant ( $\tau_R$ ) corresponding to damping a  
648 temperature perturbation relative to the radiative equilibrium state, having a FWHM of one  
649 pressure scale height (Fig. 6). This time constant depends somewhat on the width of the  
650 temperature perturbation and doubling the width increases its value by 25% in the  
651 stratosphere. Strobel et al. (2009) provided another estimate of a radiative timescale by  
652 dividing temperature by the cooling rate, which actually corresponds to the time decay of  
653 temperature when the solar heating is turned off starting from the radiative equilibrium state.  
654 While this timescale may be appropriate to investigate diurnal variations of temperature, it  
655 strongly overestimates the time constant associated with the damping of small temperature  
656 perturbations around the radiative equilibrium state such as those caused by gravity waves or  
657 moderate seasonal variations of insolation. Figure 6 shows that our time constant  $\tau_R$  is about a  
658 factor of 10 smaller than the timescale of Strobel et al., which is important to evaluate  
659 correctly the response of the atmosphere to e.g. seasonal forcing or planetary waves. For  
660 example, our calculation indicates that  $\tau_R$  exceeds 1 Titan year only in the first 7 km of  
661 Titan's atmosphere while Strobel et al.'s estimation would predict that it happens at all  
662 altitudes below 76 km. In the upper troposphere and tropopause region, 30-60 km,  $\tau_R$  is 0.25  
663 to 0.3 Titan year, which allows for non-negligible seasonal variations of temperature in  
664 contrast to expectations using Strobel et al.'s simpler formulation. In the stratosphere, above  
665 100 km ( $p < 10$  mbar),  $\tau_R$  is less than 0.03 Titan year (25 Titan days), so that significant  
666 seasonal temperature variations with almost no phase lag are expected.

667

668 As discussed by Flasar et al. (2014), the radiative time constant  $\tau_R$ , as we define it here, can  
669 be formally written as  $\left(\frac{\partial c(z)}{\partial T(z)}\right)^{-1}$  while Strobel et al. simply used  $\left(\frac{c(z)}{T(z)}\right)^{-1}$ . Using the cooling-  
670 to-space approximation and assuming that thermal cooling mostly occurs between the C<sub>2</sub>H<sub>2</sub>  
671 band at 729 cm<sup>-1</sup> and the CH<sub>4</sub> band at 1305 cm<sup>-1</sup>, Flasar et al. estimated that the difference  
672 between the two estimations in the stratosphere could amount to a factor between 6 and 11,  
673 roughly in agreement with the factor of ~10 we find.

674

675 The cooling-to-space approximation was used by Achterberg et al. (2011) to estimate the  
676 radiative relaxation time at 5°S in the stratosphere. While their results are a factor of 2 to 3  
677 smaller than  $\frac{T(z)}{c(z)}$ , they are still 4-5 times larger than our  $\tau_R$  (Fig. 6). Achterberg et al. only  
678 considered opacity from C<sub>2</sub>H<sub>6</sub>, C<sub>2</sub>H<sub>2</sub> and CH<sub>4</sub> and, based on Tomasko et al.'s (2008b)  
679 calculations, we estimate that the omission of other gases, and more importantly of haze,  
680 could explain a factor of 2 difference with our  $\tau_R$ . The rest is at least partly due to the use of  
681 the cooling-to-space approximation which differs from our calculations where the perturbed  
682 layer, only one scale height thick, can also significantly cool by emitting to other atmospheric  
683 layers in addition to space.

684

### 685 *5.3 Energy balance and adiabatic cooling*

686 Comparing the radiative heating and cooling rates at 20°S in March 2007 (Section 4.1), we  
687 found that the former exceeds the latter by 20-35% in the range 0.1-5 mbar. Given that the  
688 actual temperature variation is at least an order of magnitude smaller than the radiative  
689 cooling rate, conservation of energy implies an additional source of cooling to balance the  
690 heating. The vertical upward velocity required to produce this cooling is about 0.09 cm s<sup>-1</sup> at 1  
691 mbar and varies approximately as  $(\rho g)^{-1}$  from 1 to 5 mbar and as  $(\rho g)^{-0.45}$  from 1 to 0.1 mbar.

692



693 Similarly, around 6°N, a latitude least sensitive to seasonal effects, the radiative heating  
694 exceeds the radiative cooling around equinox at all altitudes. As a result, the radiative solution  
695 for the temperature profile is warmer than the observed one at all levels (Section 4.3, Fig. 7).  
696 An exception is the region around 85-90 km, where the two profiles exhibit the same  
697 temperature with equal heating and cooling rates. This is due to the presence of the nitrile  
698 haze parametrized by Anderson and Samuelson (2011) which increases the cooling rate by  
699 ~30% at this altitude. The radiative equilibrium solution without this nitrile haze would be  
700 about 4 K warmer at 85-90 km where it peaks according to Anderson and Samuelson. Above  
701 200 km, the uncertainty in the model temperature profile due the haze profile increases with  
702 height (Fig. 7). The difference between models using the lower and upper limits we fixed on  
703 the haze profile (Fig. 2) reaches ~3 K at 250 km (0.25 mbar), ~7 K at 300 km (0.09 mbar),  
704 ~13 K at 350 km (0.035 mbar) and ~15 K at 400 km (0.013 mbar). The coldest profile  
705 corresponds to the model of Doose et al. (2016) which has less aerosol density than the two  
706 other models. In fact, aerosol opacity provides both atmospheric cooling at long wavelengths  
707 and heating in the UV to near-infrared range, but the contribution to the heating dominates  
708 over that to the cooling.

709

710 To bring the model in general agreement with the Cassini/Huygens-derived profile at 6°N, we  
711 used an upward velocity profile  $w$  having  $0.04 \text{ cm s}^{-1}$  at 1 mbar, varying as  $(\rho g)^{-1}$  below the  
712 0.6-mbar level down to the troposphere, and as  $(\rho g)^{-0.92}$  between 0.6 and 0.02 mbar (for our  
713 nominal haze model). The largest discrepancy takes place at altitudes of Anderson and  
714 Samuelson's (2011) nitrile haze (85-90 km, ~15 mbar) where the model is ~5 K colder than  
715 measured by Huygens/HASI at 10°S in 2005. This velocity profile corresponds to ~ -1 to -1.5  
716 Pa per Titan day below the 0.02-mbar level (375 km), implying, from conservation of mass,  
717 no strong divergence of the vertical flux, i.e. weak variations of the latitudinal flow (black

718 lines in Fig. 9). On the other hand, above the 0.02-mbar level, the vertical mass flux in this  
719 model is no longer approximately conserved and diverges horizontally in latitude. Note  
720 however that the velocity profile above  $\sim 220$  km (0.5 mbar) is relatively uncertain due to  
721 uncertainties in the haze opacity profile. Using our lower limit for the haze density profile a  
722 significant divergence of the vertical mass flow is needed at much lower levels,  $\sim 1$  mbar  
723 (Fig. 9). Also, although the nominal velocity profile allows us to reproduce generally well the  
724 temperature profile retrieved at  $6^\circ\text{N}$ , discrepancies of a few degrees remain in places. For  
725 example, the temperature gradient in the model from 1 to 0.1 mbar is not steep enough.

726

727 To fit more precisely the CIRS-derived temperatures from 4 to 0.2 mbar (Fig.14), we used a  
728 slightly different vertical variation of the velocity profile with a maximum, expressed in  
729 pressure units, at 0.4-1 mbar (185-225 km), decreasing above and, more slowly, below this  
730 pressure range (thin and dashed lines in Fig. 11). This would imply (weak) convergence of the  
731 vertical flow below this region, and divergence above, a feature generally consistent with the  
732 upwelling branch of a Hadley cell (e.g. Lora et al. 2015). The two velocity profiles, derived  
733 from fitting of the  $6^\circ\text{N}$  profile retrieved by Vinatier et al. (2015) and of the CIRS temperature  
734 maps at selected levels (Fig. 15), differ by at most 40% in the 4-0.2 mbar pressure range (at 1  
735 mbar,  $0.040 \text{ cm s}^{-1}$  vs.  $0.055 \text{ cm s}^{-1}$ ). This difference lies in the uncertainty area indicated in  
736 Fig. 9 and results from small systematic differences (typically 1-3 K) in the retrievals from  
737 Achterberg et al. (in preparation) and Vinatier et al. (2015). These differences partly result  
738 from the use of different sets of spectra (respectively nadir spectra at  $2.8\text{-cm}^{-1}$  resolution and a  
739 combination of nadir and limb spectra at  $0.5\text{-cm}^{-1}$  resolution) and the different vertical  
740 resolution of the retrievals.

741

742 *5.4 Seasonal variations of temperatures from 0.2 to 4 mbar*

743 At equatorial latitudes, we found that the modulation of solar heating due to Saturn's orbital  
744 eccentricity is large enough to explain the  $\sim 4$  K drop between pre-equinox (2006-2008) and  
745 mid-2016 temperature at 1 mbar. The Sun-Saturn distance increased from 9.2 to 10.0 AU  
746 between January 2007 and January 2017, causing a decrease in insolation of 17%. This  
747 induces radiatively a  $\sim 7$  K drop in the 1-mbar temperature (Fig. 10). To reduce this drop to  
748 the observed variation, a modulation of the adiabatic cooling is needed, with less cooling after  
749 equinox than before. Assuming for simplicity a  $\sin(L_s)$  variation for this modulation, the  
750 upward velocity at 1 mbar in our best fit model varies between 0.035 and 0.075  $\text{cm s}^{-1}$  over a  
751 Titan year.

752

753 At  $30^\circ\text{S}$  and  $30^\circ\text{N}$ , we also find that our radiative model with no modulation of the adiabatic  
754 cooling considerably overestimates the observed seasonal variation at all pressure levels  
755 between 0.2 and 4 mbar. Assuming that the vertical velocity at a given level is an affine  
756 function of  $\sin(L_s)$  (Eq. 8) and that its vertical variation is the same at all latitudes, the  
757 observed variations of temperature are relatively well reproduced with the parameters listed in  
758 Table 1. An exception is the 4-mbar temperatures at the equator and  $30^\circ\text{N}$ , which show a  
759 steady decrease with time since the beginning of the Cassini mission. Such a variation cannot  
760 be reproduced with our simple radiative-dynamical model and would require a functional  
761 form for the time variation of the vertical velocity more complex than assumed in Eq. 8.

762

763 Our model shows that the time variation of the adiabatic cooling acts to counterbalance the  
764 seasonal variations of solar heating, with enhanced upwelling in summer. The modulation is  
765 stronger at  $30^\circ\text{S}$  than at  $30^\circ\text{N}$ , likely because the seasonal variations of solar heating are more  
766 pronounced in the southern hemisphere than in the northern one due to the eccentricity of  
767 Saturn's orbit, perihelion occurring less than a year after southern summer solstice. At the

768 equator, the relatively weak modulation of the adiabatic cooling (~35%) acts to mitigate the  
769 variation of solar heating due to the eccentricity, with enhanced adiabatic cooling in northern  
770 winter / southern summer when the Sun-Saturn distance is smaller. At 30°N and more  
771 significantly at 30°S, our model predicts downwelling, and thus compressional heating,  
772 around winter solstice. At 30°S, the predicted maximum downward velocity at 0.5-1 mbar is  
773  $0.05 \text{ cm s}^{-1}$ . This value is actually close to the downward velocity of  $0.06 \text{ cm s}^{-1}$  at 1 mbar  
774 required to balance the radiative cooling of  $0.06 \text{ K day}^{-1}$  derived by Teanby et al. (2017) near  
775 80°S in January 2016. This would imply that, around winter solstice, subsidence is not limited  
776 to winter polar latitudes but extends equatorward to at least  $\sim 30^\circ$ . Conversely, around  
777 equinox, for  $L_s$  between approximately  $320^\circ$  and  $30^\circ$ , upwelling occurs over the whole  
778 latitude range  $30^\circ\text{S}$ - $30^\circ\text{N}$ .

779

## 780 **6. Conclusions**

781 We have developed a one-dimensional seasonal radiative-dynamical model of Titan's  
782 atmosphere to investigate the temporal variations of Titan's stratospheric temperatures  
783 observed from 2004 to 2016 by Cassini/CIRS. This model calculates the radiative forcing  
784 using gas and haze vertical opacity profiles constrained by Cassini/CIRS and Huygens/DISR  
785 measurements. Adiabatic heating and cooling can occur by introducing a vertical velocity ( $w$ )  
786 in the energy equation. Applying this model to low latitudes, we conclude that:

- 787 • The heating and cooling rate profiles we obtained at  $20^\circ\text{S}$  are in good agreement with  
788 those calculated by Tomasko et al. (2008b). While the heating and cooling rates both  
789 decrease by a factor of  $\sim 20$  from 0.1 to 5 mbar, the heating rate constantly exceeds the  
790 cooling rate by 20-35% over this range. We find that the net radiative heating minus  
791 cooling rate steadily increase with height from the troposphere up to 250 km, in  
792 contrast with Tomasko et al. (2008b) who suggested a maximum near 120 km.

- 793 • The radiative time constant ( $\tau_R$ ) associated with the damping of a small temperature  
794 perturbation, one-scale height broad, is typically one order of magnitude shorter than  
795 that simply estimated by dividing the temperature by the cooling rate (Strobel et al.  
796 2009). Our radiative time constant is also significantly shorter than that estimated by  
797 Achterberg et al. (2011) using the cooling-to-space approximation and neglecting  
798 aerosol emission. We find that  $\tau_R$  exceeds  $10^9$  s (i.e. a Titan year) only in the first half  
799 scale height of Titan's atmosphere, contrary to previous estimations. Above the 5-  
800 mbar level,  $\tau_R$  is so short, less than 0.02 Titan year, that the solar heating rate and  
801 radiative plus dynamical cooling rate are essentially balanced at any time.
- 802 • At  $6^\circ\text{N}$  around equinox, where seasonal variations should be at minimum, we find that,  
803 as at  $20^\circ\text{S}$ , the heating rate exceeds the cooling rate at all altitudes and the radiative  
804 solution profile is thus warmer than the observed one. Adding adiabatic cooling with  
805 an upward velocity of  $\sim -1$  to  $-1.5$  Pa / Titan day (in pressure units) up to 375 km (0.02  
806 mbar), brings the model profile in general agreement with the observed one. The  
807 corresponding velocity  $w$  varies thus approximately as the inverse of the atmospheric  
808 density in this range, with  $w \sim 0.03$ - $0.05$  cm s $^{-1}$  at 1 mbar (185 km) and reaching its  
809 maximum, of the order of 1 cm s $^{-1}$ , around 0.01 mbar (415 km). Our model is however  
810 affected by uncertainties in the haze density profile above  $\sim 225$  km.
- 811 • Variations of solar heating due to Saturn's orbit eccentricity are more than sufficient  
812 to cause the decrease of equatorial temperatures observed from pre-equinox to 2016.  
813 A weak seasonal modulation of  $w$  ( $\sim 35\%$ ) is needed to bring the radiative model  
814 variation ( $\sim 7$  K at 1 mbar) near the observed one ( $\sim 4$  K at 1 mbar). This modulation  
815 reduces the adiabatic cooling during northern summer, i.e. when the Sun-Saturn  
816 distance is larger, and enhances it during southern summer.

817 • The seasonal variations predicted by the radiative model with constant-with-time  
818 adiabatic cooling are also much larger than observed at 30°S and 30°N. A simple  
819 modulation of the vertical velocity profile as an affine function of  $\sin(L_s)$  is capable of  
820 correctly reproducing the observed variations. While the required year-averaged  
821 velocity is upward (providing adiabatic cooling) at 0, 30°S and 30°N, subsidence is  
822 predicted to occur around winter solstice at 30°S and marginally at 30°N. At 1 mbar,  
823  $w$  varies in the range 0.035–0.075 cm s<sup>-1</sup> at the equator, -0.05 –0.16 cm s<sup>-1</sup> at 30°S and  
824 -0.01–0.14 cm s<sup>-1</sup> at 30°N along a Titan year.

825

826 These results may serve as a guide to general Circulation Models of Titan, which generally  
827 incorporate a less precise treatment of the radiative forcing. Although our radiative cooling  
828 and heating profiles are constrained by Cassini/Huygens observations, they still suffer from  
829 uncertainties in the haze opacity profile in the upper stratosphere and mesosphere. In  
830 particular, we have not considered variations with season of the haze profile at low latitudes,  
831 such as the evolution of the detached haze layer. We have also neglected the small seasonal  
832 variations of gaseous composition that may occur at 30°N or S. Nevertheless, the information  
833 given here should provide the basic radiative forcing at low latitudes for dynamical models.

834

835 We plan to extend this analysis to high latitudes where strong seasonal variations of  
836 composition and temperature are observed (e.g. Teanby et al. 2012, Vinatier et al. 2015,  
837 Coustenis et al. 2016, Teanby et al. 2017). The strong enhancement of photochemical species  
838 that takes place in the stratosphere during winter strongly affects the cooling rate profile and  
839 thus potentially the temperature profile. They clearly must be taken into account to  
840 characterize the adiabatic heating needed to balance the net radiative cooling, especially  
841 during the polar night.

842

843

844

845

846 **Acknowledgments**

847 BB and SV acknowledge support from the Centre National d'Études Spatiales (CNES) and

848 the Programme National de Planétologie (INSU/CNRS). RKA was supported by the NASA

849 Cassini Project. We thank the two referees whose thorough reviews helped to improve the

850 paper.

851 **References**

852

853 Achterberg, R. K., Conrath, B. J., Gierasch, P. J., Flasar, F. M., Nixon, C. A., 2008a. Titan's  
854 middle-atmospheric temperatures and dynamics observed by the Cassini Composite Infrared  
855 Spectrometer. *Icarus* 194, 263-277. doi: 10.1016/j.icarus.2007.09.029.

856

857 Achterberg, R. K., Conrath, B. J., Gierasch, P. J., Flasar, F. M., Nixon, C. A., 2008b.  
858 Observation of a tilt of Titan's middle-atmospheric superrotation. *Icarus* 197, 549-555. doi:  
859 10.1016/j.icarus.2008.05.014.

860

861 Achterberg, R. K., Gierasch, P. J., Conrath, B. J., Flasar, F. M., Nixon, C. A., 2011. Temporal  
862 variations of Titan's middle-atmospheric temperatures from 2004 to 2009 observed by  
863 Cassini/CIRS. *Icarus* 211, 686-698. doi: 10.1016/j.icarus.2010.08.009.

864

865 Anderson, C. M., Samuelson, R. E., 2011. Titan's aerosol and stratospheric ice opacities  
866 between 18 and 500  $\mu\text{m}$ : Vertical and spectral characteristics from Cassini CIRS. *Icarus* 212,  
867 762-768. doi: 10.1016/j.icarus.2011.01.024.

868

869 Bézard, B., Coustenis, A., McKay, C. P., 1995. Titan's stratospheric temperature asymmetry:  
870 A radiative origin? *Icarus* 113, 267-276. doi: 10.1006/icar.1995.1023.

871

872 Bézard, B., Nixon, C. A., Kleiner, I., Jennings, D. E., 2007. Detection of  $^{13}\text{CH}_3\text{D}$  on Titan.  
873 *Icarus* 191, 397-400. doi: 10.1016/j.icarus.2007.06.004.

874



875 Coustenis, A., et al., 2013. Evolution of the stratospheric temperature and chemical  
876 composition over one Titanian year. *Astrophys. J.* 779, id. 177, 9 pp. doi: 10.1088/0004-  
877 637X/779/2/177.

878

879 Coustenis, A., et al., 2016. Titan's temporal evolution in stratospheric trace gases near the  
880 poles. *Icarus* 270, 409-420. doi: 10.1016/j.icarus.2015.08.027.

881

882 De Kok, R., et al., 2007. Oxygen compounds in Titan's stratosphere as observed by Cassini  
883 CIRS. *Icarus* 186, 354-363. doi: 10.1016/j.icarus.2006.09.016.

884

885 Doose, L. R., Karkoschka, E., Tomasko, M. G., Anderson, C. M., 2016. Vertical structure and  
886 optical properties of Titan's aerosols from radiance measurements made inside and outside  
887 the atmosphere. *Icarus* 270, 355-375. doi: 10.1016/j.icarus.2015.09.039.

888

889 Flasar, F. M., Conrath, B. J. 1990. Titan's stratospheric temperatures: A case for dynamical  
890 inertia? *Icarus* 85, 346-354. doi: 10.1016/0019-1035(90)90122-P.

891

892 Flasar, F. M., et al., 2004. Exploring the Saturn system in the thermal infrared: The  
893 Composite Infrared Spectrometer. *Space Sci. Rev.* 115, 169–297. doi: 10.1007/s11214-004-  
894 1454-9.

895

896 Flasar, F. M., Achterberg, R. K., Schinder, P. J., 2014. Thermal structure of Titan's  
897 troposphere and middle atmosphere. In: Müller-Wodarg, I., Griffith, C. A., Lellouch, E.,  
898 Cravens, T. E. (Eds.), *Titan – Interior, Surface, Atmosphere and Space Environment*.  
899 Cambridge University Press, New York NY, pp. 102–121 (Chapter 3).

900

901 Fulchignoni, M., et al., 2005. In situ measurements of the physical characteristics of Titan's  
902 environment. *Nature* 438, 785-791. doi: 10.1038/nature04314.

903

904 Hirtzig, M., et al., 2013. Titan's surface and atmosphere from Cassini/VIMS data with  
905 updated methane opacity. *Icarus* 226, 470-486. doi: 10.1016/j.icarus.2013.05.033.  
906 Corrigendum: *Icarus* 226, 1182. doi: 10.1016/j.icarus.2013.07.015.

907

908 Irwin, P. G. J., Calcutt, S. B., Taylor, F. W., Weir, A. L., 1996. Calculated *k* distribution  
909 coefficients for hydrogen- and self-broadened methane in the range 2000-9500 cm<sup>-1</sup> from  
910 exponential sum fitting to band-modelled spectra. *J. Geophys. Res.* 101, E11, 26137-26154.  
911 doi: 10.1029/96JE02707.

912

913 Jacquemart, D., et al., 2008. New laboratory measurements of CH<sub>4</sub> in Titan's conditions and a  
914 reanalysis of the DISR near-surface spectra at the Huygens landing site. *Planet. Space Sci.* 56,  
915 613-623. doi: 10.1016/j.pss.2007.10.008.

916

917 Jacquinet-Husson, N., et al., 2011. The 2009 edition of the GEISA spectroscopic database. *J.*  
918 *Quant. Spectrosc. Radiat. Trans.* 112, 2395-2445. doi: 10.1016/j.jqsrt.2011.06.004.

919

920 Karkoschka, E., Lorenz, R. D., 1997. Latitudinal variation of aerosol sizes inferred from  
921 Titan's shadow. *Icarus* 125, 369-379. doi: 10.1006/icar.1996.5621.

922

923 Karkoschka, E., Tomasko, M. G., 2010. Methane absorption coefficients for the jovian  
924 planets from laboratory, Huygens, and HST data. *Icarus* 205, 674-694. doi:  
925 10.1016/j.icarus.2009.07.044.  
926

927 Karkoschka, E., Schröder, S. E., Tomasko, M. G., Keller, H. U., 2012. The reflectivity  
928 spectrum and opposition effect of Titan's surface observed by Huygens' DISR spectrometers.  
929 *Planet. Space Sci.* 60, 342-355. doi: 10.1016/j.pss.2011.10.014.  
930

931 Landau, L., Lifchitz, E., 1969. *Physique théorique. Tome I. Mécanique.* 3<sup>rd</sup> edition (revised).  
932 Ed. MIR, Moscow.  
933

934 Lebonnois, S., Burgalat, J., Rannou, P., Charnay, B., 2012. Titan global climate model: A  
935 new 3-dimensional version of the IPSL Titan GCM. *Icarus* 218, 707-722. doi:  
936 10.1016/j.icarus.2011.11.032.  
937

938 Lebonnois, S., Flasar, F. M., Tokano, T., Newman, C. E., 2014. The general circulation of  
939 Titan's lower and middle atmosphere. In: Müller-Wodarg, I., Griffith, C. A., Lellouch, E.,  
940 Cravens, T. E. (Eds.), *Titan – Interior, Surface, Atmosphere and Space Environment.*  
941 Cambridge University Press, New York NY, pp. 122–157 (Chapter 4).  
942

943 Lellouch, E., et al., 2014. The distribution of methane in Titan's stratosphere from  
944 Cassini/CIRS observations. *Icarus* 231, 323-337. doi: 10.1016/j.icarus.2013.12.016.  
945

946 Lora, J. M., Lunine, J. I., Russell, J. L. 2015. GCM simulations of Titan's middle and lower  
947 atmosphere and comparison to observations. *Icarus* 250, 516-528. doi:  
948 10.1016/j.icarus.2014.12.030.

949

950 Newman, C. E., Lee, C., Lian, Y., Richardson, M. I., Toigo, A. D., 2011. Stratospheric  
951 superrotation in the TitanWRF model. *Icarus* 213, 636-654. doi: 10.1016/j.icarus.2011.03.025.  
952

953 Niemann, H. B., et al., 2010. Composition of Titan's lower atmosphere and simple surface  
954 volatiles as measured by the Cassini-Huygens probe gas chromatograph mass spectrometer  
955 experiment. *J. Geophys. Res.* 115, E12006. doi: 10.1029/2010JE003659.

956

957 Press, W. H., Teukolsky, S. A., Vetterling, W. T., Flannery, B. P., 1997. *Numerical Recipes in*  
958 *Fortran 77: The Art of Scientific Computing* (Vol. 1 of Fortran Numerical Recipes).  
959 Cambridge Univ. Press, New York NY (Chapter 15).

960

961 Rey, M., Nikitin, A. V., Bézard, B., Rannou, P., Coustenis, A., Tyuterev, V. G., 2017. New  
962 accurate theoretical line lists of  $^{12}\text{CH}_4$  and  $^{13}\text{CH}_4$  in the 0-13400  $\text{cm}^{-1}$  range: Application to  
963 the modelling of methane absorption in Titan's atmosphere. *Icarus*, submitted.

964

965 Rothman, L. S., et al., 2013. The HITRAN2012 molecular spectroscopic database. *J. Quant.*  
966 *Spectrosc. Radiat. Trans.* 130, 4-50. doi: 10.1016/j.jqsrt.2013.07.002.

967

968 Stamnes, K., Tsay, S-C., Wiscombe, W., Jayaweera, K., 1988. Numerically stable algorithm  
969 for discrete-ordinate-method radiative transfer in multiple scattering and emitting layered  
970 media. *Appl. Opt.* 27, 2502-2509. doi: 10.1364/AO.27.002502.

971

972 Strobel, D. F., et al., 2009. Atmospheric structure and composition. In: Brown, R. H.,  
973 Lebreton, J.-P., Waite, J. H. (Eds.), Titan from Cassini-Huygens. Springer, Dordrecht, pp.  
974 235–257 (Chapter 10).

975

976 Teanby, N. A., et al., 2007. Vertical profiles of HCN, HC<sub>3</sub>N, and C<sub>2</sub>H<sub>2</sub> in Titan's atmosphere  
977 derived from Cassini/CIRS data. *Icarus* 186, 364-384. doi: 10.1016/j.icarus.2006.09.024.

978

979 Teanby, N. A., et al., 2008. Global and temporal variations in hydrocarbons and nitriles in  
980 Titan's stratosphere for northern winter observed by Cassini/CIRS. *Icarus* 193, 595-611. doi:  
981 10.1016/j.icarus.2007.08.017.

982

983 Teanby, N. A., Irwin, P. G. J., de Kok, R., Nixon, C. A. 2009. Dynamical implications of  
984 seasonal and spatial variations in Titan's stratospheric composition. *Phil. Trans. Royal Soc.*  
985 367, 697-711. doi: 10.1098/rsta.2008.0164.

986

987 Teanby, N. A., et al., 2012. Active upper-atmosphere chemistry and dynamics from polar  
988 circulation reversal on Titan. *Nature* 491, 732-735. doi: 10.1038/nature11611.

989

990 Teanby, N. A., et al., 2017. The formation and evolution of Titan's winter polar vortex. *Nat.*  
991 *Commun.*, in press.

992

993 Tomasko, M. G., Bézard, B., Doose, L., Engel, S., Karkoschka, E., 2008a. Measurements of  
994 methane absorption by the descent imager/spectral radiometer (DISR) during its descent  
995 through Titan's atmosphere. *Planet. Space Sci.* 56, 624-647. doi: 10.1016/j.pss.2007.10.009.

996

997 Tomasko, M. G., Bézard, B., Doose, L., Engel, S., Karkoschka, E., Vinatier, S., 2008b. Heat  
998 balance in Titan's atmosphere. *Planet. Space Sci.* 56, 648-659. doi: 10.1016/j.pss.2007.10.012.  
999

1000 Tomasko, M. G., et al., 2008c. A model of Titan's aerosols based on measurements made  
1001 inside the atmosphere. *Planet. Space Sci.* 56, 669-707. doi: 10.1016/j.pss.2007.11.019.  
1002

1003 Vinatier, S., et al., 2007. Vertical abundance profiles of hydrocarbons in Titan's atmosphere at  
1004 15° S and 80° N retrieved from Cassini/CIRS spectra. *Icarus* 188, 120-138. doi:  
1005 10.1016/j.icarus.2006.10.031.  
1006

1007 Vinatier, S., et al., 2010a. Analysis of Cassini/CIRS limb spectra of Titan acquired during the  
1008 nominal mission. I. Hydrocarbons, nitriles and CO<sub>2</sub> vertical mixing ratio profiles. *Icarus* 205,  
1009 559-570. doi: 10.1016/j.icarus.2009.08.013.  
1010

1011 Vinatier, S., et al., 2010b. Analysis of Cassini/CIRS limb spectra of Titan acquired during the  
1012 nominal mission. II: Aerosol extinction profiles in the 600-1420 cm<sup>-1</sup> spectral range. *Icarus*  
1013 210, 852-866. doi: 10.1016/j.icarus.2010.06.024.  
1014

1015 Vinatier, S., Rannou, P., Anderson, C. A., Bézard, B., de Kok, R., Samuelson, R. E., 2012.  
1016 Optical constants of Titan's stratospheric aerosols in the 70-1500 cm<sup>-1</sup> spectral range  
1017 constrained by Cassini/CIRS observations. *Icarus* 219, 5-12. doi:  
1018 10.1016/j.icarus.2012.02.009.  
1019

1020 Vinatier, S., et al., 2015. Seasonal variations in Titan's middle atmosphere during the northern  
1021 spring derived from Cassini/CIRS observations. *Icarus* 250, 95-115. doi:  
1022 10.1016/j.icarus.2014.11.019.  
1023  
1024 Vinatier, S., et al., 2016. Seasonal variations in Titan's stratosphere observed with  
1025 Cassini/CIRS after the northern spring equinox. American Astronomical Society, DPS  
1026 meeting #48, id.509.09.  
1027  
1028 Vinatier, S., et al., 2017a. Study of Titan's fall southern stratospheric polar cloud composition  
1029 with Cassini/CIRS: detection of benzene ice. *Icarus*, submitted.  
1030  
1031 Vinatier, S., et al., 2017b. Seasonal variations in Titan's stratosphere observed with  
1032 Cassini/CIRS during northern spring. American Astronomical Society, DPS meeting #49,  
1033 id.304.03.